

1-1-1982

The Effect of the Sr/Ti Ratio and Additives on the Microstructure and Electrical Conductivity of SrTiO₃.

Stefan R. Witek

Follow this and additional works at: <http://preserve.lehigh.edu/etd>

 Part of the [Materials Science and Engineering Commons](#)

Recommended Citation

Witek, Stefan R., "The Effect of the Sr/Ti Ratio and Additives on the Microstructure and Electrical Conductivity of SrTiO₃." (1982). *Theses and Dissertations*. Paper 2323.

This Thesis is brought to you for free and open access by Lehigh Preserve. It has been accepted for inclusion in Theses and Dissertations by an authorized administrator of Lehigh Preserve. For more information, please contact preserve@lehigh.edu.

The Effect of the Sr/Ti Ratio and
Additives on the Microstructure and
Electrical Conductivity of SrTiO₃

by

Stefan R. Witek

A Thesis

Presented to the Graduate Committee
of Lehigh University
in Candidacy for the Degree of
Master of Science
in the Department of
Metallurgy and Materials Engineering

Lehigh University

1982

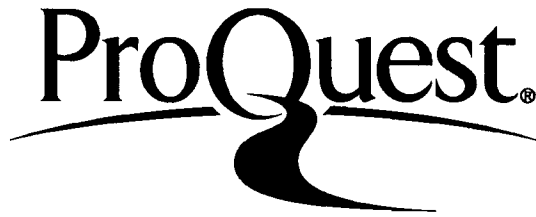
ProQuest Number: EP76599

All rights reserved

INFORMATION TO ALL USERS

The quality of this reproduction is dependent upon the quality of the copy submitted.

In the unlikely event that the author did not send a complete manuscript and there are missing pages, these will be noted. Also, if material had to be removed, a note will indicate the deletion.



ProQuest EP76599

Published by ProQuest LLC (2015). Copyright of the Dissertation is held by the Author.

All rights reserved.

This work is protected against unauthorized copying under Title 17, United States Code
Microform Edition © ProQuest LLC.

ProQuest LLC.
789 East Eisenhower Parkway
P.O. Box 1346
Ann Arbor, MI 48106 - 1346

This thesis is accepted and approved in partial fulfillment of the requirements for the degree of Master of Science.

Sept 7, 1982
Date

Professor in Charge

Chairman of Department

ACKNOWLEDGEMENTS

I would like to thank Dr. D. M. Smyth for his help and guidance, and Dr. M. P. Harmer, Al Walker and my fellow graduate students for their helpful suggestions and discussions. I am very grateful to Jeanne Loosbrock for typing this thesis. I acknowledge the financial support of the National Science Foundation.

TABLE OF CONTENTS

	<u>Page</u>
List of Tables	v
List of Figures	vii
Abstract	1
Chapter	
I Introduction	3
II Experimental	20
III Results and Discussion	29
IV Conclusions	72
Bibliography	76
Appendix - Tables of Conductivity Data	78
Vita	103

LIST OF TABLES

<u>Table</u>		<u>Page</u>
1a.	Ionic Radii of Cations in ABO_3 Perovskites and Some Potential Dopants	19
1b.	Impurity Behaviour in $BaTiO_3$ and $SrTiO_3$ (Lee's Work).	56
2.	Samples Investigated as a Continuation of Lee's Work.	57
3.	Impurity Behaviour in $BaTiO_3$ and $SrTiO_3$ (including this study).	58
4.	The Conductivity Data for ST1.005-1405Al	79
5.	The Conductivity Data for ST1.005-1132Sc	80
6.	The Conductivity Data for BT1.005-1284Al	81
7.	The Conductivity Data for BT1.005-1124Nb	82
8.	The Conductivity Data for BT1.002-844La	83
9.	The Conductivity Data for ST1.000-Undoped	84
10.	The Conductivity Data for ST1.000-Undoped	85
11.	The Conductivity Data for ST0.995-Undoped	86
12.	The Conductivity Data for ST0.995-Undoped	87
13.	The Conductivity Data for ST0.995-Undoped	88
14.	The Conductivity Data for ST0.990-Undoped	89
15.	The Conductivity Data for ST0.900-Undoped	90
16.	The Conductivity Data for ST0.810-Undoped	91
17.	The Conductivity Data for ST1.002-Undoped	92
18.	The Conductivity Data for ST1.005-Undoped	93
19.	The Conductivity Data for ST1.005-10000Al	94
20.	The Conductivity Data for ST0.995-10000Al	95
21.	The Conductivity Data for BT0.995-10000Al	96

<u>Table</u>		<u>Page</u>
22.	The Conductivity Data for ST0.995-10000Nb	97
23.	The Conductivity Data for ST0.995-5000NB	98
24.	The Conductivity Data for ST0.995-15000Nb	99
25.	The Conductivity Data for ST0.995-20000Nb	100
26.	The Conductivity Data for ST0.995-30000Nb	101
27.	The Conductivity Data for ST0.995-2000Nb	102

LIST OF FIGURES

<u>Figure</u>		<u>Page</u>
1.	Log σ vs log PO_2 for undoped and Al-doped $SrTiO_3$ (Chan's results).	15
2.	Schematic representation of equilibrium defect model for undoped and acceptor-doped $SrTiO_3$ (17).	16
3.	Log σ vs log PO_2 for Nb-doped $SrTiO_3$ (Chan's results).	17
4.	Schematic representation of equilibrium defect model for donor-doped $SrTiO_3$ (19).	18
5.	Sample for 4-point d.c. conductivity measurement.	23
6.	System used for 4-point d.c. conductivity measurement.	23
7.	Schematic diagram of conductivity measuring equipment.	26
8.	Schematic diagram of zirconia cell.	27
9a.	Scanning electron micrograph of polished and acid-etched sample with $Sr/Ti = 0.900$, slow-cooled from $1400^\circ C$.	38
9b.	Scanning electron micrograph of polished and acid-etched sample with $Sr/Ti = 0.900$, slow-cooled from $1400^\circ C$.	38
10a.	Energy dispersive spectrum of large second phase particle shown in Figure 9a.	39
10b.	Energy dispersive spectrum of matrix shown in Figure 9a.	39
10c.	Energy dispersive spectrum of small second phase particle shown in Figure 9a.	39
11.	$SrO-TiO_2$ phase diagram (29).	40

<u>Figure</u>	<u>Page</u>
12a. Scanning electron micrograph of polished and acid-etched sample with Sr/Ti = 0.810, slow-cooled from 1400°C.	41
12b. Scanning electron micrograph of polished and acid-etched sample with Sr/Ti = 0.810, slow-cooled from 1400°C.	41
12c. Scanning electron micrograph of polished and acid-etched sample with Sr/Ti = 0.810, quenched from 1470°C.	41
12d. Energy dispersive spectrum of large second phase particle shown in Figure 12c.	41
13a. Scanning electron micrograph of polished and acid-etched sample with Sr/Ti = 0.995, slow-cooled from 1400°C.	42
13b. Scanning electron micrograph of polished and acid-etched sample with Sr/Ti = 0.995, quenched from 1400°C.	42
13c. Scanning electron micrograph of acid-etched "hole" in sample with Sr/Ti = 0.995, quenched from 1400°C.	42
13d. Scanning electron micrograph of acid-etched "hole" in sample with Si/Ti = 0.995, quenched from 1470°C.	42
14a. Scanning electron micrograph of polished and acid-etched sample with Sr/Ti = 1.000, slow-cooled from 1400°C.	43
14b. Scanning electron micrograph of polished and thermally-etched sample with Sr/Ti = 1.000, slow-cooled from 1400°C.	43
15. Log σ vs log PO ₂ for undoped SrTiO ₃ .	44
16. Log σ vs log PO ₂ for undoped SrTiO ₃ .	45
17. Log σ vs log PO ₂ for undoped SrTiO ₃ .	46
18. Log σ vs log PO ₂ for undoped SrTiO ₃ .	47

<u>Figure</u>	<u>Page</u>
19. Log σ vs log PO_2 for undoped $SrTiO_3$.	48
20. Log σ vs log PO_2 for Al- and Sc-doped $SrTiO_3$.	59
21. Log σ vs log PO_2 for Al-doped $BaTiO_3$.	60
22. Log σ vs. log PO_2 for Nb- and La-doped $BaTiO_3$.	61
23. Log σ vs log PO_2 for Al-doped $SrTiO_3$.	64
24. Log σ vs log PO_2 for Al-doped $BaTiO_3$.	65
25. Log σ vs log PO_2 for Nb-doped $SrTiO_3$.	69
26. Scanning electron micrograph of acid-etched "hole" in sample with $Sr/(Ti+Nb) = 0.995$, doped with 2000 ppm Nb.	70
27. Scanning electron micrograph of acid-etched "hole" in sample with $Sr/(Ti+Nb) = 0.995$, doped with 5000 ppm Nb.	70
28. Scanning electron micrograph of acid-etched "hole" in sample with $Sr/(Ti+Nb) = 0.995$, doped with 10000 ppm Nb.	70
29. Scanning electron micrograph of polished and acid-etched sample with $Sr/(Ti+Nb) = 0.995$, doped with 15000 ppm Nb.	70
30. Scanning electron micrograph of polished and acid-etched sample with $Sr/(Ti+Nb) = 0.995$, doped with 20000 ppm Nb.	71

ABSTRACT

Results of high temperature equilibrium electrical conductivity measurements as a function of oxygen partial pressure have been analysed for Al- and Sc-doped polycrystalline SrTiO_3 and Al-, Nb-, and La-doped polycrystalline BaTiO_3 using a defect model that includes only V_{Sr}'' (or V_{Ba}''), V_{O}'' , electrons, holes, and impurities. It has been found that BaTiO_3 and SrTiO_3 both exhibit acceptor-type behaviour when doped with Al or Sc, regardless of the respective Ba/Ti or Sr/Ti ratios. Nb- and La-doped BaTiO_3 with Ba/Ti > 1 show para-donor-type behaviour.

Scanning electron microscopy of polished and etched samples of polycrystalline SrTiO_3 reveal the presence of a second phase, apparently TiO_2 , when Sr/Ti \leq 0.995 (mol % $\text{TiO}_2 \geq 50.125$). The amount of second phase increases with the amount of excess TiO_2 . When the samples are cooled rapidly from the sintering temperature, the second phase particles are fewer in number and smaller. Based on a defect model for SrTiO_3 , the position of the minimum equilibrium conductivity as a function of oxygen partial pressure is a convenient measure of the relative content of extrinsic V_{O}'' , i.e. those due to impurities and/or excess TiO_2 . The observed conductivity results are consistent with a slight solubility of excess TiO_2 .

in SrTiO_3 . The effect of cooling rate indicates that exsolution of TiO_2 can occur during some part of the cooling process, while the stability of the conductivity curves at 1000°C indicates that resolution does not occur at this temperature.

The same defect model has been applied to equilibrium conductivity results for SrTiO_3 containing excess SrO , and BaTiO_3 and SrTiO_3 doped with 10000 ppm Al. It appears that excess SrO has a limited solubility in SrTiO_3 , and that Al is much more soluble in SrTiO_3 than in BaTiO_3 .

Acceptor-type, donor-type, and para-donor-type behaviour have all been observed in Nb-doped SrTiO_3 , depending on the concentration of Nb. Scanning electron micrographs show some evidence to support the proposed defect models.

CHAPTER I

INTRODUCTION

In recent years SrTiO_3 has received a great deal of attention due to its useful electrical properties (1,2,3). The properties of sintered polycrystalline SrTiO_3 depend upon its microstructure. The sintering variables, such as temperature and composition, are chosen so as to reproduce a desirable microstructure in the most convenient and inexpensive way. All the basic transport processes that occur in oxides, including sintering and electrical conductivity, are determined by the relative movement of atoms and electrons throughout the material considered. The common factor in all of these processes is the existing defect structure, and therefore an understanding of the defects that are present and their behaviour is of great importance to the transport processes. For example, it has been quite well established that doubly ionized oxygen vacancies and related electrons are the major defects in both pure and acceptor-doped SrTiO_3 under reduced conditions, and that oxygen vacancies have some mobility at ambient temperatures (4,5, 6,7). Many of the important electrical phenomena such as dielectric degradation (8) are dependent upon the concentrations and relative mobilities of electrons and oxygen vacancies.

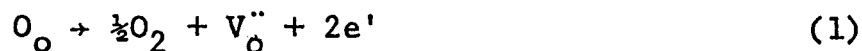
A common method of determining the defect structure is to measure electrical conductivity as a function of

oxygen activity in the solid. The conductivity, σ_i , is related to the charge carrier concentration, n_i , and its mobility, μ_i , by the relation $\sigma_i = n_i q_i \mu_i$, where q_i is the charge on the carrier. As the oxygen activity is altered, variations in the concentration, n_i , with changes in the defect structure are reflected in the conductivity.

All of the practical applications for SrTiO_3 lie at a temperature well below the sintering temperature. Since thermodynamic equilibrium cannot be attained for this oxide at the operating temperature, the defects present are those which were retained during cooling from the sintering temperature. It is therefore of great value to study the defect structure of the material at an elevated temperature.

The equilibrium defect chemistry of BaTiO_3 has been studied in considerable detail as a result of its application as a ferroelectric and piezoelectric material (9-16). Chan et al. (17) have found the defect structure of SrTiO_3 to be similar to that of BaTiO_3 . Their electrical conductivity results have been correlated by means of a model in which the doubly ionized oxygen vacancy, V_O'' , is the key defect and for which three major sources are postulated. The defect notation is that developed by Kröger and Vink (18).

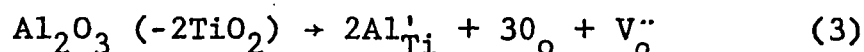
Reduction or loss of oxygen:



Cation nonstoichiometry in the sense of excess TiO_2 :



The incorporation of acceptor-type impurities such as substitution of Al_2O_3 for $2TiO_2$:



For undoped and acceptor-doped $SrTiO_3$, the complete expression for the condition of charge neutrality is:

$$2[V_o''] + p = 2[V_{Sr}''] + [A'] + n \quad (4)$$

where $[A']$ represents the net acceptor content, both accidental and added, expressed as the equivalent concentration of single-level acceptor centres, $n \equiv [e']$, and $p \equiv [h^{\cdot}]$.

An example of a conductivity plot for undoped $SrTiO_3$ obtained by Chan et al. is shown in Fig. 1. This plot of conductivity against oxygen partial pressure can be divided into three characteristic regions depending on whether the $SrTiO_3$ has a stoichiometric deficiency or excess of oxygen, and depending on which terms in eqn. (4) are most important. The following analysis (17) is very similar to that proposed for $BaTiO_3$ (9,10,14,16), and a schematic representation of the defect model is shown in Fig. 2.

Region I -- In the region of lowest PO_2 , the material is oxygen deficient and the reduction reaction, Eq. (1), is the major source of defects. The approximate condition of charge neutrality is thus

$$2[V_O^{\bullet\bullet}] \approx n \quad (5)$$

The mass-action expression for the reduction reaction is

$$[V_O^{\bullet\bullet}]n^2 = k_1 PO_2^{-1/2} \quad (6)$$

Combination of Eq. (5) and (6) leads to

$$n \approx (2k_1)^{1/3} PO_2^{-1/6} \quad (7)$$

which agrees with the PO_2 dependence of the electron concentration found by Yamada and Miller (4) and of conductivity found by Walters and Grace (6). The agreement between the PO_2 dependence of the conductivity and the electron concentration found by these two groups indicates that the electron mobility is not composition dependent under these conditions. It will be shown that our own results barely reach into Region I at the lowest PO_2 and exhibit this PO_2 dependence in a very limited region, which is also the case with Chan's results as shown in Fig. 1.

Region II -- This region is bounded on the low PO_2 side by Region I and on the high PO_2 side by the conductivity minima. The pressure dependence of the conductivity is approximately $PO_2^{-1/4}$ which indicates oxygen-

deficient, n-type behaviour. This PO_2 dependence for the electron concentration can be obtained from the mass-action expression for the reduction reaction, Eq. (6), if $[V_O^{\bullet\bullet}]$ is independent of PO_2 , i.e., if there is an extrinsic source of $V_O^{\bullet\bullet}$ such that the reduction reaction is no longer the major source of $V_O^{\bullet\bullet}$. This could be due to either excess TiO_2 or to acceptor impurities, Eq. (2) and (3). In this model it is proposed that even in undoped material with $Sr/Ti = 1.000$, there is sufficient accidental net excess of acceptor impurities to control $[V_O^{\bullet\bullet}]$ in this region. Only in the region of lowest PO_2 does the reduction reaction, Eq. (1), become the major source of $V_O^{\bullet\bullet}$. The preponderance of acceptor impurities is related to the relative natural abundances of such impurity elements as compared to donor impurity elements. The approximate condition of charge neutrality is then

$$[V_O^{\bullet\bullet}] = [V_{Sr}^{\bullet\bullet}] + \frac{1}{2} A' \quad (8)$$

where $[V_{Sr}^{\bullet\bullet}]$ represents the contribution to $[V_O^{\bullet\bullet}]$ made by excess TiO_2 , while $\frac{1}{2}[A']$ is the contribution made by the net excess acceptor content. The sum of these two contributions is referred to as the extrinsic $V_O^{\bullet\bullet}$ content. Combination of eq. (6) and (8) gives

$$n = \left\{ \frac{k_1}{[V_{Sr}^{\bullet\bullet}] + \frac{1}{2}[A']} \right\}^{\frac{1}{2}} PO_2^{-\frac{1}{2}} \quad (9)$$

This PO_2 dependence is characteristic of a wide region of the experimental results, as shown in the example in Fig. 1.

Region III -- This is the oxygen excess, p-type region lying between the conductivity minima and $PO_2 \cong 1$ atm. The stoichiometric excess of oxygen is accommodated by the extrinsic V_O'' present because of a net excess of acceptor impurities or an excess of TiO_2



Thus there is no crystallographic excess of oxygen and no need to propose such unfavorable defects as O_i'' or V_{Ti}'''' . This is in accord with the very modest enthalpy of oxygen addition as indicated by the small temperature dependence of conductivity in this region (17). The approximate condition of charge neutrality is the same as in Region II, Eq. (8), as long as a negligible fraction of the extrinsic V_O'' is consumed by the oxygen excess. Combination of the mass-action expression for Eq. (10)

$$\frac{p^2}{[V_O'']} = k_{10} PO_2^{-\frac{1}{2}} \quad (11)$$

with Eq. (8) gives

$$p = k_{10}^{\frac{1}{2}} \{ [V_{Sr}'''] + \frac{1}{2}[A'] \}^{\frac{1}{2}} PO_2^{\frac{1}{4}} \quad (12)$$

This is a good representation of the PO_2 dependence of conductivity observed in this region (Fig. 1).

The Conductivity Minima -- the conductivity minima correspond to the p-n transitions where the electron and hole contributions to the conductivity are equal

$$n\mu_n = p\mu_p \quad (13)$$

where μ_n and μ_p are the electron and hole mobilities. At the point of exact compensation, which is offset from the conductivity minimum by the mobility ratio, the only source of carriers is by ionization across the bandgap.

$$\text{nil} \rightleftharpoons e' + h' \quad (14)$$

$$np = k_{14} = k'_{14} e^{-E_g^0/kT} \quad (15)$$

where nil refers to the standard state with all electrons in the lowest available energy states, and E_g^0 is the bandgap at 0 K or the enthalpy of the ionization reaction, Eq. (14). At the point of compensation

$$n = p = (k'_{14})^{1/2} e^{-E_g^0/2kT} \quad (16)$$

The effects of excess TiO_2 and acceptor impurities -- By combination of Eq. (9) and (12), the PO_2 at the minimum, $\text{PO}_2(\text{min.})$, can be expressed as

$$\begin{aligned} \text{PO}_2(\text{min.}) &= \left(\frac{\mu_n}{\mu_p}\right)^2 \frac{k_1}{k_{10}} \frac{1}{\{[V_{\text{Sr}}''] + \frac{1}{2}[A']\}^2} \\ &= \left(\frac{\mu_n}{\mu_p}\right)^2 \frac{k_1}{k_{10}} \frac{1}{[V_{\text{O}}'']_{\text{ext}}^2} \end{aligned} \quad (17)$$

where $[V_{\text{O}}'']_{\text{ext}}$ is the extrinsic V_{O}'' concentration. The shift of $\text{PO}_2(\text{min.})$ with $[V_{\text{O}}'']_{\text{ext}}$ is independent of the mobilities.

$$\frac{d \log \text{PO}_2(\text{min.})}{d \log [V_{\text{O}}'']_{\text{ext}}} = -2 \quad (18)$$

Thus at a given temperature, the minimum moves to lower PO_2 by two orders of magnitude for each order of magnitude increase in V_O'' ext, and this shift serves as a measure of the relative extrinsic V_O'' contents of various samples. This parameter is independent of the absolute values of the conductivity and thus of the sample geometry and density. An example of this type of shift in the minimum due to acceptor doping is shown in Fig. 1. It is also represented schematically in Fig. 2.

Donor-doped $SrTiO_3$ has been studied by Chan et al. (17), and by Lee (19). Fig. 3 shows conductivity plots for Nb-doped $SrTiO_3$ samples obtained by Chan et al. The schematic representation of the defect model is shown in Fig. 4, and is divided into two regions.

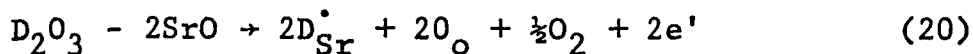
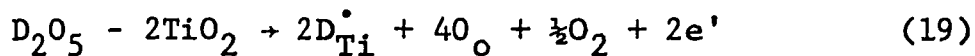
Region I -- The reduction reaction, Eq. (1), is the major source of defects. The carrier concentration has the same dependence on the oxygen partial pressure as in Region I of the acceptor-doped material, i.e.

$$n \approx (2k_1)^{1/3} PO_2^{-1/6} \quad (7)$$

This PO_2 dependence is observed in the conductivity results at low PO_2 for all the samples shown in Fig. 4.

Region II -- Two types of donors are considered here: D_2O_5 where the Ti is substituted for by a pentavalent (D^{+5}) cation, and D_2O_3 where the Sr is substituted for by a trivalent (D^{+3}) cation. The donors are compensated

by electrons according to the following equations:



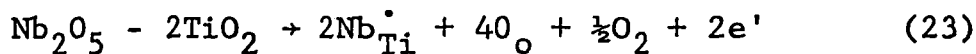
The approximate conditions of charge neutrality are

$$[\text{D}_{\text{Ti}}^\bullet] \approx n \quad (21)$$

$$\text{or } [\text{D}_{\text{Sr}}^\bullet] \approx n \quad (22)$$

The carrier concentration is fixed by the donor dopant during the sample preparation. Therefore an oxygen pressure independence of electrical conductivity is observed.

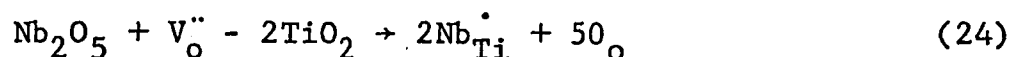
Figure 3 shows profiles for samples containing 498 ppm Nb. The sample with Sr/Ti = 1.000 behaves very much as expected from the model described above. There is a PO_2 -independent region corresponding to the following equation.



The expulsion of the fifth oxygen from the filled lattice leaves free electrons which compensate the charged donor centres. This leads to a region of impurity-controlled PO_2 -independent electron concentration and conductivity.

In the case of Sr/Ti = 0.999, with a dopant concentration of 498 ppm Nb, the conductivity is significantly reduced in the impurity-controlled region. When Sr/Ti = 0.995, with the same dopant concentration, the donor-doped behaviour is lost completely and the conductivity profile

looks very much like that of an undoped sample. The loss of the donor-doped characteristics is supposedly due to the increase in $V_{\text{O}}^{\bullet\bullet}$ content with the amount of excess TiO_2 (see equation (2)). The extra oxygen carried by the Nb_2O_5 can therefore be accommodated in the lattice until finally it is all retained and the characteristic donor-type behaviour is no longer observed, as shown here:



Thus by altering the composition of SrTiO_3 , it is possible to vary the concentration of various defects within the material. These changes can then be studied using high temperature electrical conductivity measurements.

Chan et al. (9.17) have measured the effect of excess TiO_2 on the electrical conductivity of BaTiO_3 and SrTiO_3 . From the results it appears that there is some solubility of excess TiO_2 (<0.5 mol %) in SrTiO_3 , and that TiO_2 is practically insoluble in BaTiO_3 . Eror and Balachandran (25) report that the oxygen pressure dependence of electrical conductivity in samples with $\text{Sr}/\text{Ti} = 0.996, 0.99, \text{ and } 0.98$ were found to be similar to that obtained in strontium titanate with ideal cation-cation ratio. They suggest the results indicate that SrTiO_3 does not saturate with TiO_2 even at 50.505 mol % and this is in disagreement with the results of Chan et al. (17) who predicted that the phase boundary for single-phase SrTiO_3 is less than

50.1 mol % TiO_2 .

In our research the effect of the Sr/Ti ratio on electrical conductivity of SrTiO_3 has been investigated and compared to the results of Chan et al. (17) and Eror and Balachandran (25). The microstructures of several samples have been studied using the scanning electron microscope, and these have been related to their corresponding conductivity results and defect models. The microstructural results have been compared to similar observations in BaTiO_3 by Sharma et al. (22).

The effect of various dopants on the electrical conductivity of SrTiO_3 and BaTiO_3 have been studied as a continuation of Lee's work (19). Based solely on the consideration of the relative ionic size (Table 1a), the Nb^{+5} , Al^{+3} , and Sc^{+3} ions are assumed to occupy the Ti site and La^{+3} and Y^{+3} ions are assumed to substitute for the Ba or Sr. Al- and Sc-doping should therefore result in acceptor-type behaviour since Al'_{Ti} and Sc'_{Ti} defects are formed respectively, whereas Nb-, Y-, and La-doping is expected to give donor-type behaviour with the formation of $\text{Nb}^{\bullet}_{\text{Ti}}$, $\text{Y}^{\bullet}_{\text{Sr}}$ or $\text{Y}^{\bullet}_{\text{Ba}}$, and $\text{La}^{\bullet}_{\text{Sr}}$ or $\text{La}^{\bullet}_{\text{Ba}}$, respectively.

Changing the Sr/Ti or Ba/Ti ratio is expected to produce an effect upon the impurity behaviour in SrTiO_3 or BaTiO_3 ; for example, the presence of excess TiO_2 may force a trivalent impurity that normally occupies the Ti site to substitute for Sr or Ba and give rise to donor-

type behaviour, whereas in the presence of excess SrO or BaO, the trivalent impurity may substitute for Ti which would result in acceptor-type behaviour. This seems particularly feasible in the case of trivalent impurity ions whose sizes are intermediate between those of Ti and Sr or Ba. The effect of the Sr/Ti and Ba/Ti ratios on the impurity behaviour in SrTiO₃ and BaTiO₃ was therefore investigated.

Changes in conductivity as a result of additions to SrTiO₃ of up to 10,000 ppm Al have been studied and compared with results obtained for BaTiO₃.

The effect of various concentrations of Nb (up to 30,000 ppm) on the conductivity of SrTiO₃ has been examined. Both acceptor- and donor-type behaviour have been observed depending on the dopant concentration. Microstructures of Nb-doped samples have been studied on the scanning electron microscope, and have been related to the electrical conductivity results and defect equations.

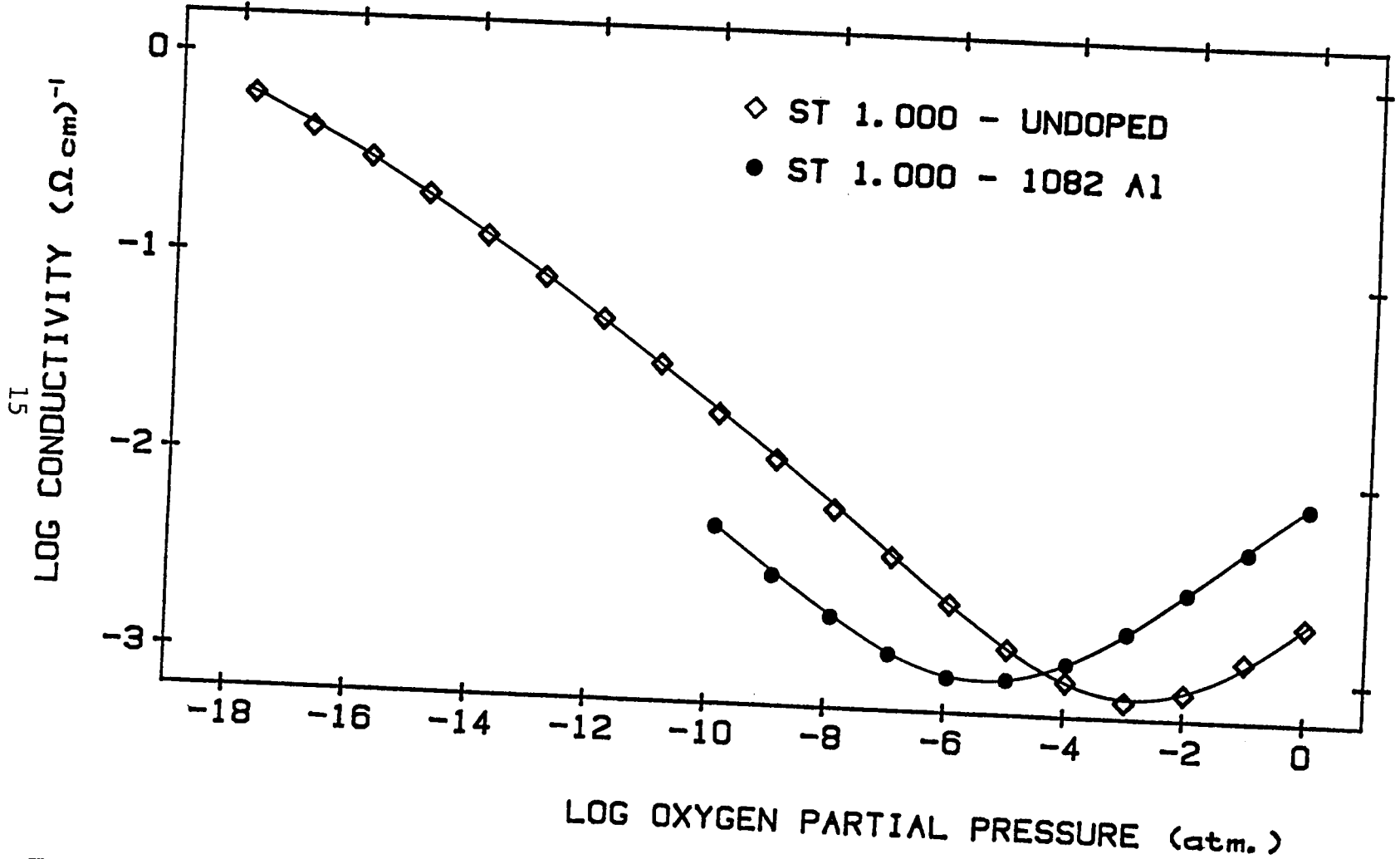


FIGURE 1 : LOG σ vs LOG P_{O_2} FOR UNDOPED & Al-DOPED SrTiO₃ (Chan)

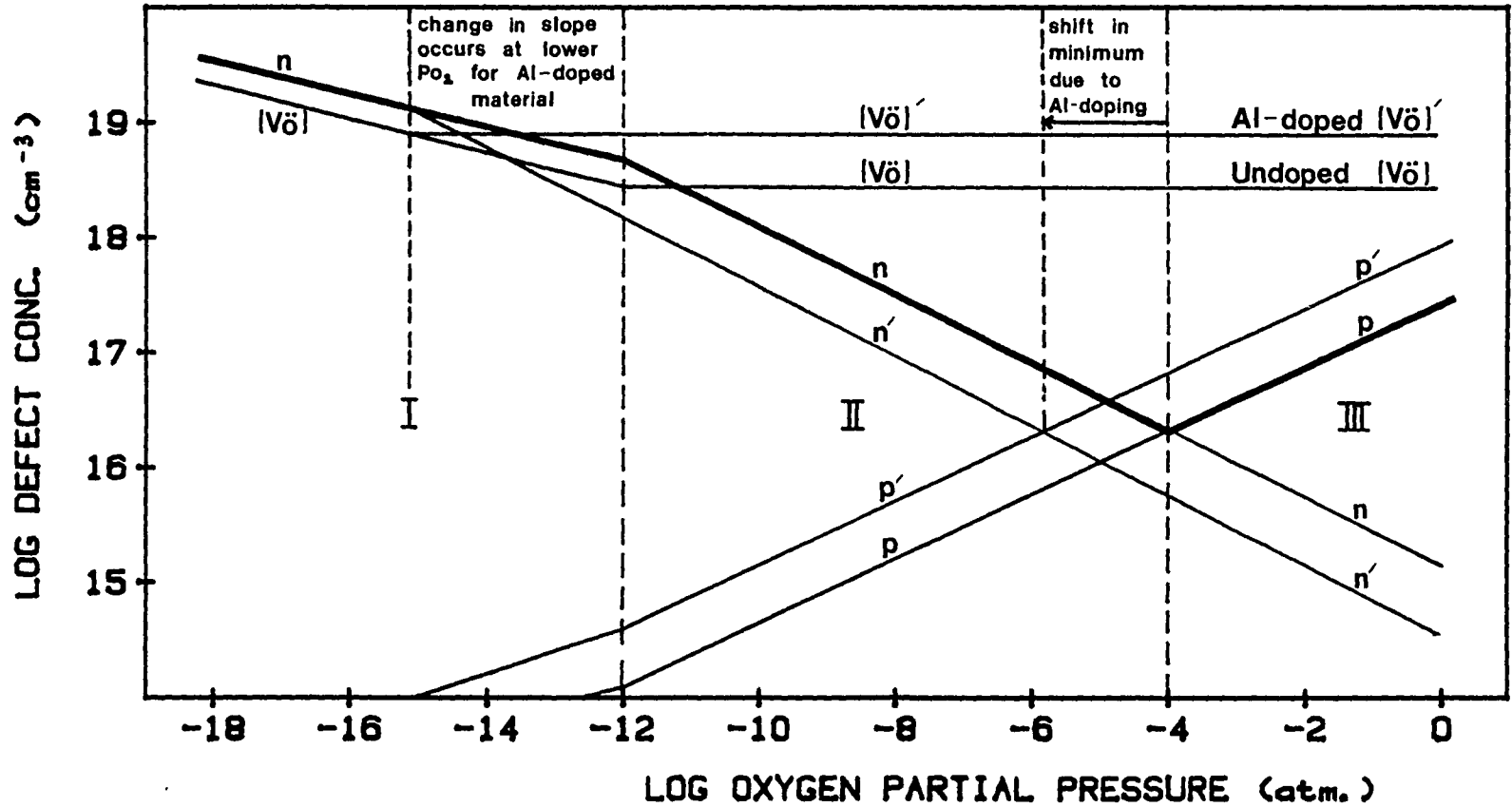


FIGURE 2 , SCHEMATIC REPRESENTATION OF EQUILIBRIUM DEFECT MODEL FOR UNDOPED AND ACCEPTOR - DOPED SrTiO_3 (17)

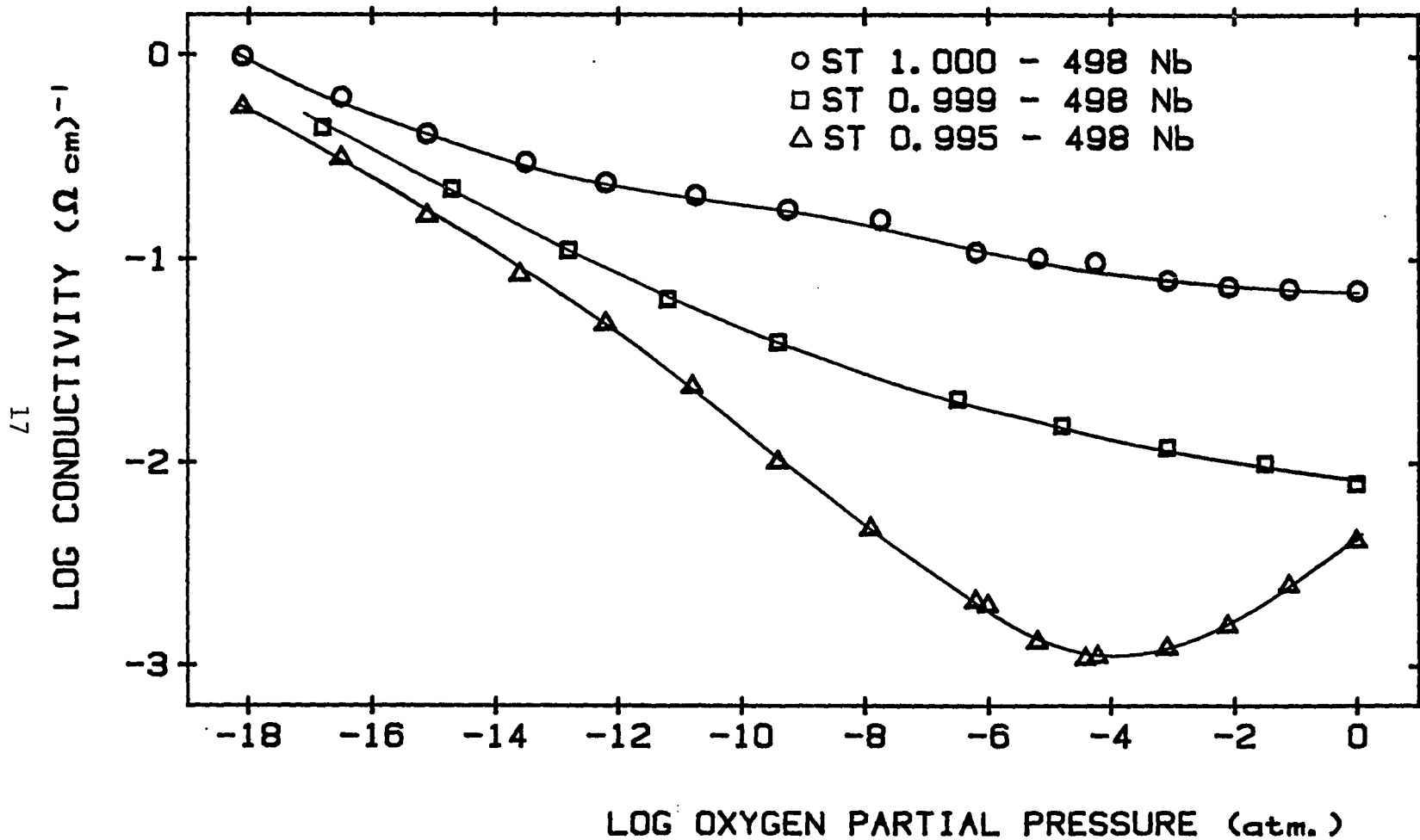


FIGURE 3 : LOG σ vs LOG P_{O_2} FOR Nb-DOPED $SrTiO_3$ (Chan's results)

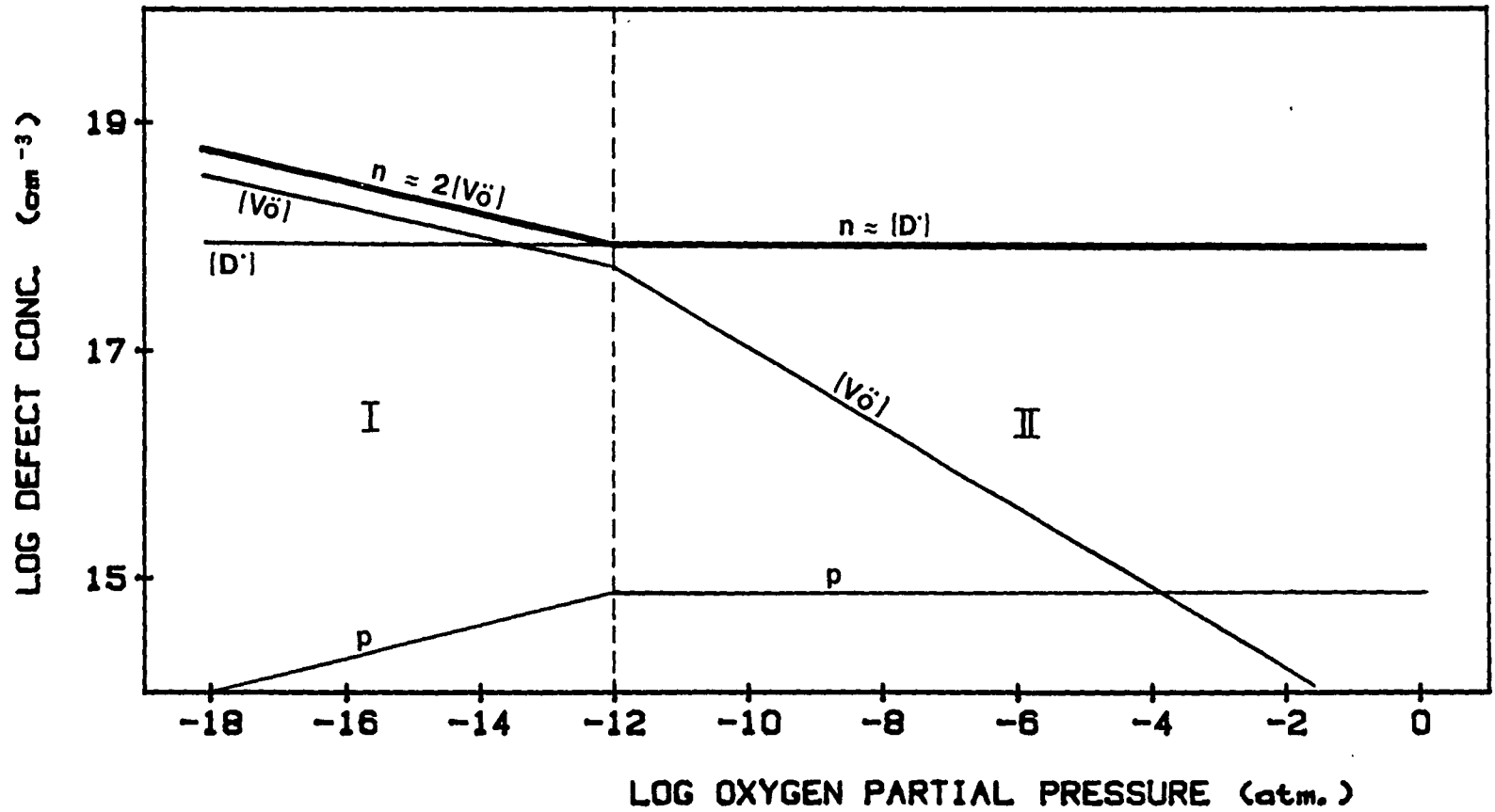


FIGURE 4 : SCHEMATIC REPRESENTATION OF EQUILIBRIUM DEFECT MODEL FOR DONOR - DOPED SrTiO_3 (19)

TABLE 1a. Ionic Radii of Cations in ABO_3 Perovskites
and Some Potential Dopants (26)

Cations	Ba ⁺²	Sr ⁺²	Ti ⁺⁴	Nb ⁺⁵	Al ⁺³	La ⁺³	Y ⁺³	Sc ⁺³
Å	1.50	1.27	0.745	0.78	0.67	1.185	1.04	0.885

CHAPTER II

EXPERIMENTAL

1. Sample Preparation

SrTiO_3 samples were prepared by a modification of a technique developed by Pechini (20), described by Chan et al. (17). Several liters of titanium stock solution were prepared by combining batches made in the following way: 200 ml of tetra-iso-propyl orthotitanate, obtained from E. I. du Pont de Nemours as Tyzor "TPT," was added with stirring to 2 liters of Fisher Certified ethylene glycol; 350 g of Fisher Certified ACS anhydrous citric acid was added and the mixture was stirred until complete solution was achieved. It was then treated until the strong odor of isopropyl alcohol disappeared. Presumably during this procedure the isopropoxy groups attached to the titanium are replaced by the multifunctional ethylene glycol, which can thermally polymerize with the multifunctional citric acid by an esterification reaction. After the combined batches had been allowed to homogenize for two weeks in a polyethylene container, weighed samples were thermally polymerized and ignited to TiO_2 to determine the Ti content of the solution, which was 0.055649 g TiO_2 /g solution. Donor- and acceptor-dopant solutions were prepared by solution of niobium oxalate obtained as a 10% solution from Kawecki-Berylco, and Eastman

practical grade tri-iso-propyl aluminate, respectively, in ethylene glycol. Both solutions were assayed by the ignition of weighed portions to the corresponding oxide.

The source of Sr was Johnson-Matthey specpure SrCO_3 , reported to contain 5 ppm Ba, 2 ppm Fe, 1 ppm Ag, and <1 ppm Ca, Cu, and Mg, all on a weight basis. Samples of SrTiO_3 were prepared by dissolution of weighed amounts of the SrCO_3 , dried by ignition at 950°C in CO_2 , in weighed portions of the Ti stock solution, containing weighed amounts of dopant solution where appropriate. Dissolution of the carbonate, by reaction with the citric acid content, was achieved by heating in a glass crystallizing dish on a hot plate over a period of several hours. The viscosity was kept low by additions of dilute citric acid until solution was complete. When all the carbonate had dissolved, the mixture was poured into platinum crucibles and allowed to polymerize thermally to a glassy solid by raising the temperature of the hot plate. Thus the homogeneity of the liquid solution was transformed to the solid glass without phase separation. This was then calcined in the same platinum crucible in a furnace at 900°C to yield a fine SrTiO_3 powder. The sample compositions are expressed in terms of Sr/Ti ratios where it should be understood that the Ti includes any added Al, Sc or Nb content and the Sr includes any added La content, since the dopants are assumed to occupy a

particular site depending on their size. These ratios are thus actually site occupation ratios. For example, for each gram atom of Al-dopant added, one mole of TiO_2 was left out, i.e., Al_2O_3 was substituted for 2TiO_2 . The dopant and impurity contents are expressed in ppm atomic based on Sr or Ti sites, e.g. $(\text{No. of added Al atoms} \times 10^6)/(\text{No. of Ti and added Al atoms})$.

Samples for conductivity measurements were prepared in the following way. 0.4 g samples of the powder, with 3 or 4 drops of water to improve pressability, were pressed into rectangular bars at 50,000 psi. All faces and edges were cleaned to remove contamination from the steel die. Two holes were drilled through the largest face and 2 cm lengths of platinum wire were inserted through each hole. These two wires were to serve as voltage leads. The samples were then typically sintered at 1400°C in platinum containers. They were held at 1400°C for two hours in air, and either furnace-cooled or quenched by rapidly pulling out of the furnace onto a refractory block. Thus the voltage leads were firmly fixed within the holes of the sample after sintering. Unfluxed platinum paste (Engelhard 6926) was then fired onto the ends at 900°C to serve as current leads. The finished sample is shown diagrammatically in Fig. 5.

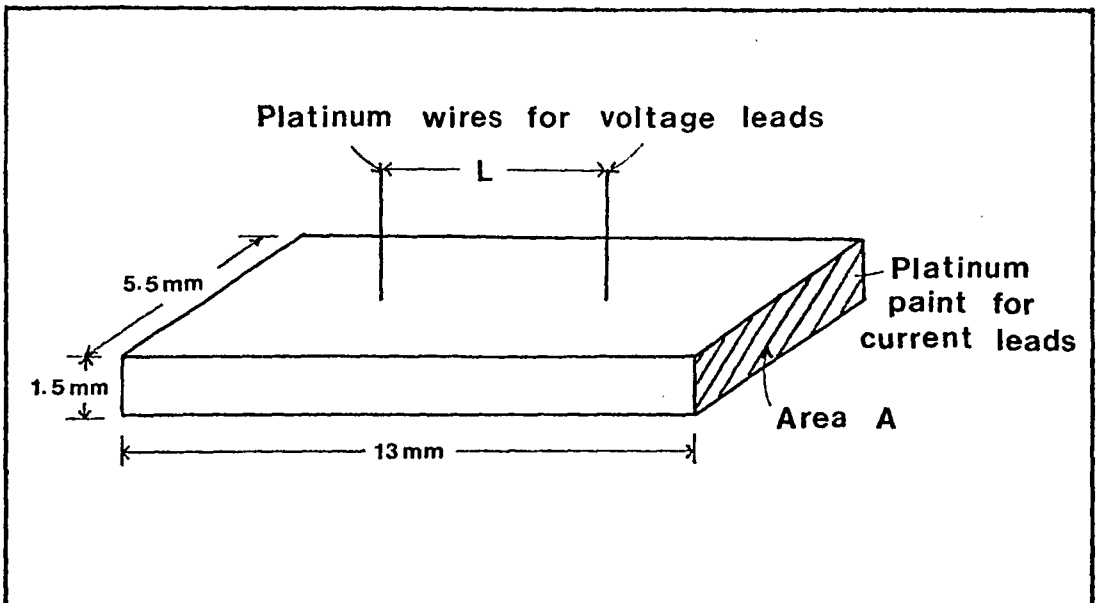


FIGURE 5: SAMPLE FOR 4-POINT D.C. CONDUCTIVITY MEASUREMENT

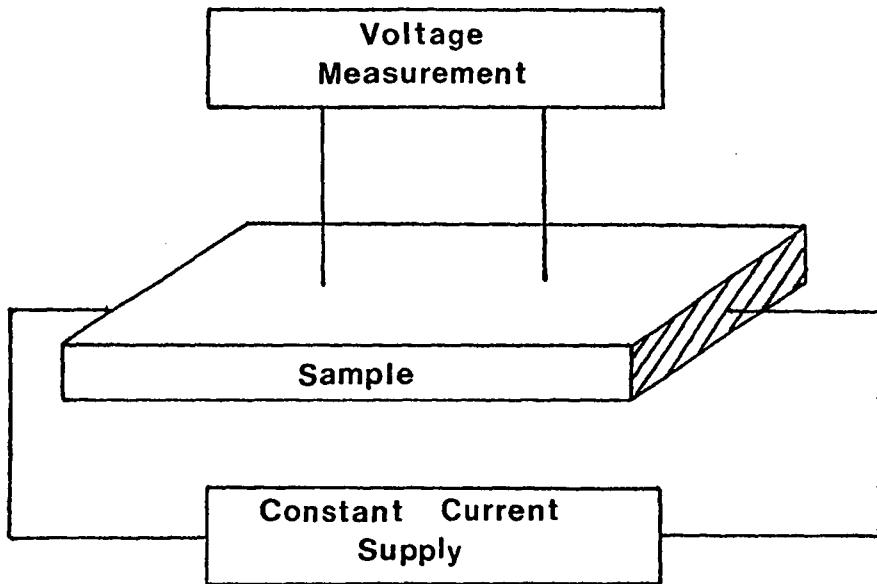


FIGURE 6: SYSTEM USED FOR 4-POINT D.C. CONDUCTIVITY MEASUREMENT

2. Conductivity Measurements

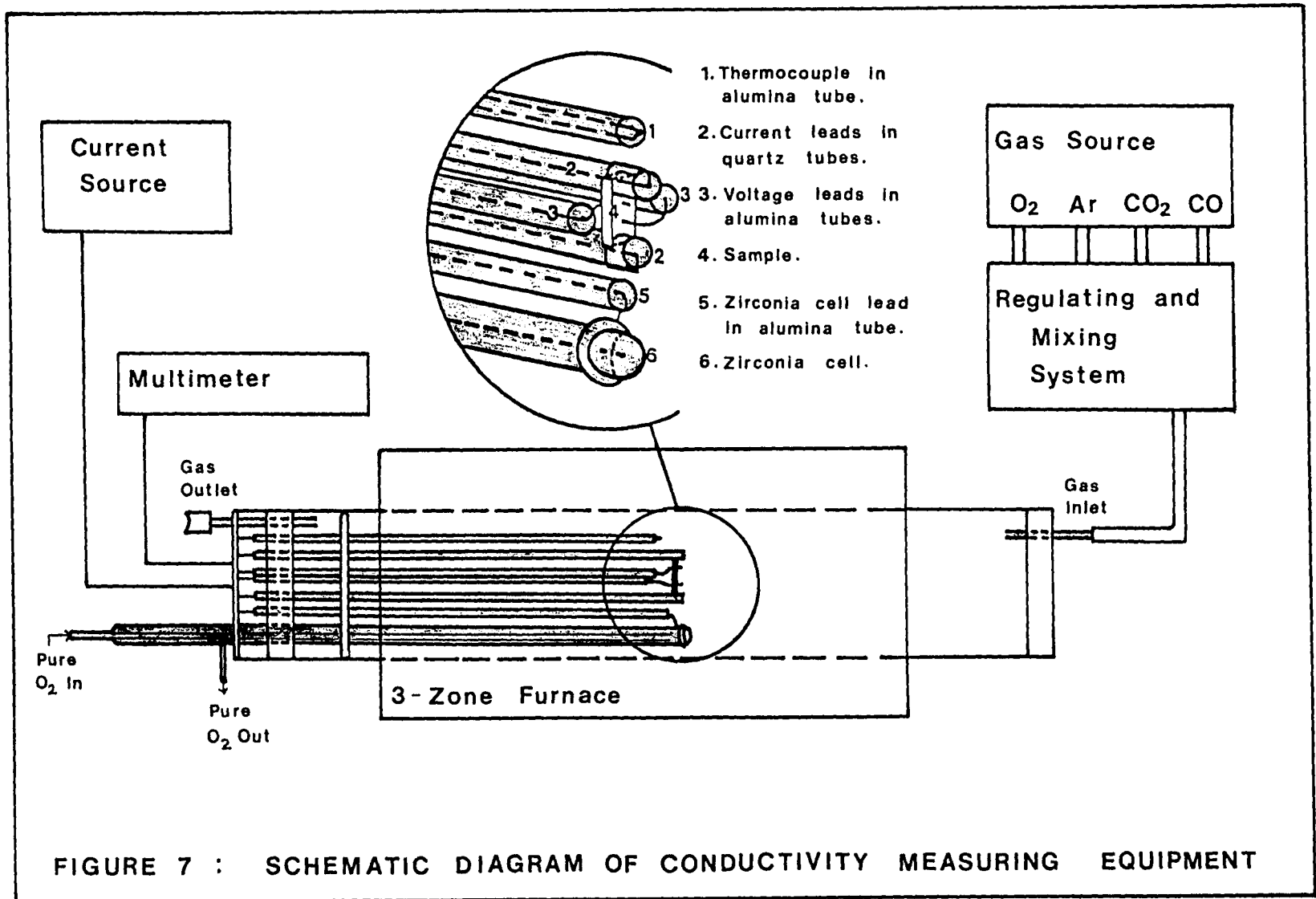
The conductivity was measured with the four-point d.c. technique, using both polarities of applied currents in the range 10^{-6} - 10^{-1} A to maintain a voltage drop of about 0.5 V. The currents were provided by a Keithley 225 current source and the voltage drops were measured using a Keithley 173A Multimeter. The four-probe conductivity technique overcomes the problem of contact resistance normally encountered in other systems (21). Figure 6 shows a schematic diagram of the system used here. If the current I through the specimen and the voltage V across the two inner probes are measured, the specimen conductivity is given by

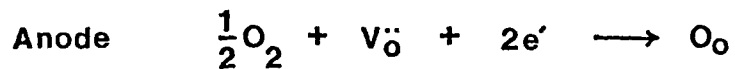
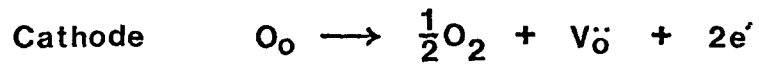
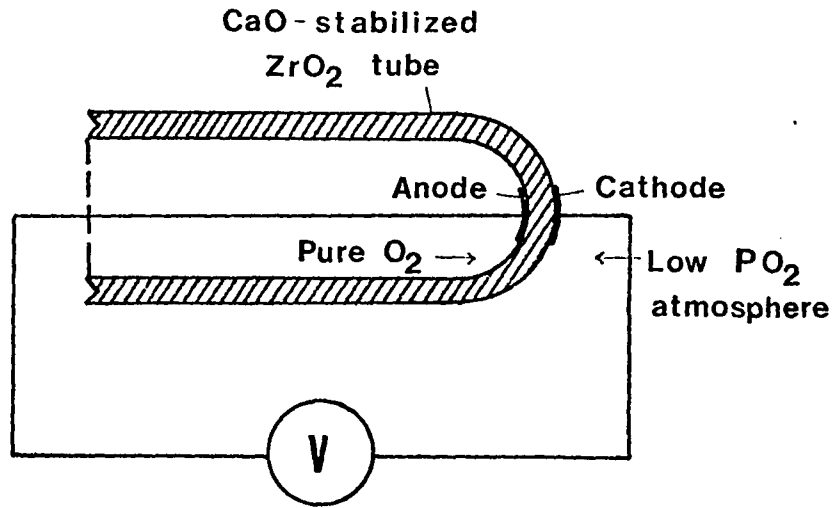
$$\sigma = \frac{IL}{VA} \quad (25)$$

where A is the cross-sectional area of the specimen and L is the separation of the two inner probes (Fig. 5). σ is in $(\text{ohm cm})^{-1}$, A in cm^2 , and L in cm. No portion of the voltage drop V occurs across the outer current contacts and, therefore, any barrier layers in the vicinity of these contacts do not affect the measured value of conductivity. With the employment of the high impedance multimeter, negligible current is allowed to flow in the voltage measurement leads. Consequently, there will be no voltage drop across the resistance associated with the voltage contacts and this resistance will not influence the conductivity measurement.

All conductivity measurements were made in a Lindberg 3-zone furnace at a temperature of 1000°C. The system is shown schematically in Fig. 7. All the levels of PO_2 were obtained by mixtures of Ar- O_2 and CO- CO_2 . The resulting oxygen activity was determined by the measurement of the emf from a CaO-stabilized ZrO_2 cell which was located adjacent to the conductivity samples. The cell consisted of a closed-end tube of stabilized zirconia, platinized inside and outside only at the tip, with the inside continuously flushed with oxygen (see Fig. 8).

One sample was measured at a time, the ends of the sample being supported by quartz tubes with platinum contacts through which the current was passed. (Quartz was used since it has a very low coefficient of thermal expansion and good contact with the sample had to be maintained during heating to 1000°C.) The voltage leads of the sample were attached to platinum wires running through separate alumina tubes. A Pt/Pt-10% Rh thermocouple was also present within another alumina tube. All the tubes were supported by a metal spacer well outside the hot zone of the furnace.





$$E = \frac{RT}{4F} \log \frac{PO_2''}{PO_2'}$$

where E = e.m.f. produced by cell

R = gas constant

T = absolute temperature

F = Faraday constant

PO_2'' & PO_2' = equilibrium partial pressures of oxygen at cathode and anode respectively

FIGURE 8 : SCHEMATIC DIAGRAM OF ZIRCONIA CELL

3. Microstructural Analysis

In order to study the microstructure of the samples, rough polishing was accomplished on SiC 600 mesh paper, followed by a final polish using diamond paste (6 μm to 0.25 μm grade). The samples were either thermally etched or chemically etched in HNO_3 with a few drops of HF. Microstructural analysis was carried out by scanning electron microscopy.

CHAPTER III

RESULTS AND DISCUSSION

3.1 The Effect of Excess TiO_2 on Microstructure and Electrical Conductivity of SrTiO_3

Figures 9a and 9b show scanning electron micrographs of a polished and etched sample having $\text{Sr/Ti} = 0.900$, which had been sintered at 1400°C and slow-cooled to room temperature. A discrete second phase is clearly observable. Its visibility is enhanced because it is more resistant to the acid etchant than is the matrix, suggesting that a higher concentration of the more basic Sr is present in the matrix. Figure 10a shows an X-ray spectrum obtained with an energy dispersive spectrometer when one of the large particles of second phase was probed with the scanning electron beam. Only Ti X-rays were detected in this case. Figure 10b shows a spectrum obtained from the matrix and indicates the presence of Sr. Figure 10c corresponds to one of the smaller particles of second phase, and also shows a small Sr peak, but it is believed that these Sr X-rays are from the surrounding matrix and are produced as a result of the limited spatial resolution of the electron beam. Stenton and Harmer (27) have examined a SrTiO_3 sample having $\text{Sr/Ti} = 0.900$ (sintered at 1400°C) using scanning transmission electron microscopic (STEM) analysis, and have found the composition of the second phase to be pure TiO_2 . This

was confirmed using electron diffraction, which showed that the second phase had the rutile structure.

Figure 11 is the phase diagram for SrO-TiO₂, which predicts a second phase of composition TiO₂ in samples containing more than 50 mol % TiO₂ sintered at 1400°C. It appears from the phase diagram that no excess TiO₂ is soluble in SrTiO₃ at all.

Figures 12a and 12b show scanning electron micrographs of a sample containing more excess TiO₂, with a Sr/Ti ratio of 0.81. The sample was sintered at 1400°C and slow cooled to room temperature. Comparing with Figs. 9a and 9b, there are more second phase particles present in this material. Figure 12c represents the same sample sintered at 1470°C (which is above the SrTiO₃-TiO₂ eutectic temperature of 1440°C) and quenched to room temperature. The particles of second phase are generally smaller in this case, and are more continuous along the grain boundaries. Figure 12d is the X-ray spectrum obtained by probing the large second phase particle shown in Fig. 12c. Thus the particle was found to be TiO₂, as was the case in samples sintered at 1400°C. STEM analysis by Stenton and Harmer (27) on a sample having Sr/Ti = 0.900, sintered at 1470°C, showed that the second phase was in the form of a continuous layer of varying thickness along the grain boundaries, and was pure TiO₂. According to the phase diagram for SrO-TiO₂ (Fig. 11), a liquid second phase

containing Sr should form if the material is sintered above the eutectic temperature. However, to observe any Sr in the second phase, the sample would have to be cooled infinitely fast, otherwise there is a possibility that SrTiO_3 forms and segregates from the liquid mixture during cooling to nucleate at the interface with the SrTiO_3 matrix and leave behind pure TiO_2 . From the morphology of the second phase in the material sintered above the eutectic temperature (Fig. 12c), it appears that the excess TiO_2 did react to form a liquid at the sintering temperature.

Figures 13a and 13b show scanning electron micrographs of two samples having $\text{Sr/Ti} = 0.995$ (or 0.5 mol % excess TiO_2) sintered at 1400°C . Figure 13a represents a slow-cooled sample and Fig. 13b represents a quenched sample. Particles of second phase are present in both materials. Their composition is assumed to be TiO_2 as in the case of the samples containing more excess TiO_2 described above. The particles are much smaller in the quenched material as shown in Fig. 13b, and were only observed in a few regions.

Figure 13c is a scanning electron micrograph of a hole in the quenched sample, showing a group of small second phase particles present at a grain boundary. (As a result of quenching, damage due to thermal shock made polishing almost impossible, resulting in the presence of

large holes throughout the material.) Figure 13d is a scanning electron micrograph of a sample also containing 0.5 mol % excess TiO_2 but sintered at 1470°C and quenched. Again large holes formed when attempts were made to polish the material. No discrete second phase particles were observed, but there appear to be some areas of second phase having a different morphology (top right hand side of Fig. 13d).

Figure 14a shows a scanning electron micrograph of a polished and acid-etched sample with $\text{Sr}/\text{Ti} = 1.000$. Figure 14b is a scanning electron micrograph of a polished and thermally-etched surface of the same sample. No second phase was observed, since no excess TiO_2 was present in this material.

It may be concluded from these microstructural results that the second phase present in samples having $\text{Sr}/\text{Ti} < 1$ is TiO_2 . The amount of second phase decreases as the Sr/Ti ratio approaches unity. In samples rapidly cooled from the sintering temperature, the second phase particles are fewer in number and smaller. Sintering at a higher temperature changes the morphology and reduces the size of the second phase particles. Thus it appears that excess TiO_2 is more soluble in SrTiO_3 at higher temperatures and more of it may be retained in solution by rapidly cooling, but the solubility limit is much less than 0.5 mol %.

Figure 15 shows the conductivity profiles obtained at 1000°C for samples having Sr/Ti = 1, which had been either slow-cooled or quenched from a sintering temperature of 1400°C. The experimental results can be correlated by means of the defect model described in the Introduction. As stated before, the minimum in the conductivity profile moves to a lower PO_2 by two orders of magnitude for each order of magnitude increase in $[V_O^{''}]_{\text{ext}}$ (Eq. (18)), and this shift serves as a measure of the relative extrinsic $V_O^{''}$ contents of various samples produced by acceptor-doping or dissolved excess TiO_2 . From Fig. 15 it can be seen that the position of the conductivity minimum is independent of cooling rate in the absence of excess TiO_2 . Figure 16 shows conductivity profiles at 1000°C for two samples of undoped $SrTiO_3$ having Sr/Ti = 0.995, together with the profiles for the stoichiometric samples shown in Fig. 15. All samples were sintered at 1400°C, but one of each composition was either slow-cooled or quenched, as indicated in Fig. 16. The conductivity minima occur at lower PO_2 for Sr/Ti = 0.995, indicating an increase in extrinsic $V_O^{''}$ content with excess TiO_2 , as expected from Eq. (2). There is a further shift of the minimum to lower PO_2 for the quenched sample having Sr/Ti = 0.995, suggesting that more of the excess TiO_2 is soluble at the sintering temperature and may be retained in solution by quenching, thus increasing the

$[V''_O]_{\text{ext}}$. No such effect of cooling rate on the position of the conductivity minimum was observed for samples with $\text{Sr/Ti} = 1.000$, which is to be expected since no excess TiO_2 should be present in those samples.

Figure 17 compares conductivity profiles obtained for samples with $\text{Sr/Ti} = 0.995$, one sintered at 1470°C and the other at 1400°C , followed by quenching in air. The conductivity minimum is at a slightly lower PO_2 for the sample sintered at the higher temperature, indicating an increase in solubility of the excess TiO_2 at the higher temperature.

The micrographs and conductivity results are consistent with a slight solubility of excess TiO_2 (<0.5 mol %) in SrTiO_3 , the solubility increasing with higher sintering temperatures. This is in agreement with the results of Chan et al. (17) but contradicts the findings of Eror and Balachandran (25) who suggest that the solubility is much higher. The effect of cooling rate indicates that exsolution of TiO_2 can occur during some part of the cooling process, while the stability of the conductivity curves at 1000°C indicates that resolution does not occur at this temperature.

Although Eror and Balachandran (25) state that much higher levels of excess TiO_2 are soluble in SrTiO_3 , their conductivity results show no shift in the minimum expected if the TiO_2 goes into solution, which they explain

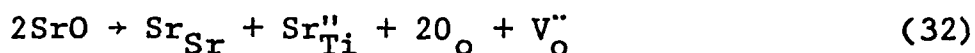
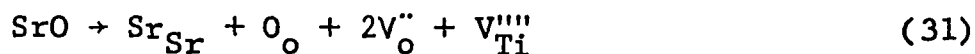
in terms of the formation of neutral vacancy pairs (V_{Sr}'' V_{O}''). However, the conductivity minimum for a stoichiometric composition obtained by Eror and Balachandran occurs at a PO_2 of approximately 10^{-5} atm. which corresponds to our results for samples containing excess TiO_2 . Our stoichiometric sample exhibited a conductivity minimum at approximately $10^{-3.5}$ in agreement with the results of Chan et al. (17). We therefore suggest that Eror and Balachandran do not observe a shift in the minimum since they have not measured a truly stoichiometric undoped composition.

Sharma et al. (22) have studied the effect of the Ba/Ti ratio on the microstructure of sintered polycrystalline BaTiO_3 , and Chan et al. (9) have measured the electrical conductivity of BaTiO_3 with various Ba/Ti ratios. Their results indicate that TiO_2 is practically insoluble in BaTiO_3 .

Figure 18 includes the conductivity profiles for samples containing larger amounts of excess TiO_2 . All samples were sintered at 1400°C and slow-cooled. The stoichiometric composition ($\text{Sr}/\text{Ti} = 1.000$) and the 0.5 mol % excess TiO_2 composition have profiles exhibiting a limited $-1/6$ dependence at the lowest PO_2 region, which indicates that the reduction reaction (Eq. (1)) is the major source of V_{O}'' at those values of PO_2 . For the less stoichiometric compositions, only a $-1/2$ dependence

is observed at lower PO_2 , since the excess TiO_2 is the major source of V_O'' according to Eq. (2). The profiles for samples having $Sr/Ti = 0.990$ and 0.900 shown in Fig. 18 are identical. The values of conductivity are higher than expected by comparison to the stoichiometric and 0.5 mol % excess TiO_2 compositions. The sample with $Sr/Ti = 0.81$ shows a further increase in conductivity in the lower region of PO_2 ($<10^{-3}$ atm.). It is proposed that this may be due to a contribution to conductivity from the larger amount of second phase present in these samples. The second phase (TiO_2) could increase the concentration of electrons at lower PO_2 according to Eq. (1). The $-1/2$ dependence is retained according to Eq. (9) for the bulk of the material, but there is an increase in the actual values of conductivity as a result of more electrons being produced by the second phase at lower PO_2 .

The effect of excess SrO on the conductivity of $SrTiO_3$ was also studied, and the profiles obtained for samples containing 0.2 mol % and 0.5 mol % excess SrO are compared with that of the stoichiometric composition in Fig. 19. There is a shift in the minimum to a lower value of PO_2 for the samples having excess SrO , as was the case with samples containing excess TiO_2 . This suggests that the excess SrO is also a source of V_O'' ext. The following equations are postulated:



Equation (32) seems more likely, since Sr_{Ti}'' would be a more energetically favorable compensating defect than V_{Ti}'''' considering its lower effective charge. Also, perovskite-type compounds with Sr ions occupying Ti sites have been listed by Galasso (28).

The same argument used for excess TiO_2 in the introduction may be applied in this case to yield an analogous equation to Eq. (9), i.e.

$$n \approx \left\{ \frac{k_1}{[\text{Sr}_{\text{Ti}}''] + \frac{1}{2}[\text{A}']} \right\}^{\frac{1}{2}} \text{PO}_2^{-\frac{1}{4}} \quad (33)$$

which again results in Eq. (18):

$$\frac{d \log \text{PO}_2(\text{min.})}{d \log [\text{V}_{\text{O}}'']_{\text{ext}}} = -2 \quad (18)$$

Thus it is believed that excess SrO also has a limited solubility in SrTiO_3 and gives rise to $\text{V}_{\text{O}}''_{\text{ext}}$. Comparing the shift in the conductivity minimum produced by 0.5 mol % excess SrO and that produced by 0.5 mol % excess TiO_2 (Figs. 16 and 19), it appears that TiO_2 is slightly more soluble than SrO in SrTiO_3 -- the V_{Sr}'' produced by excess TiO_2 is probably a more energetically favorable defect than the Sr_{Ti}'' formed by excess SrO, considering the difference in ionic radius between a Sr and Ti ion.

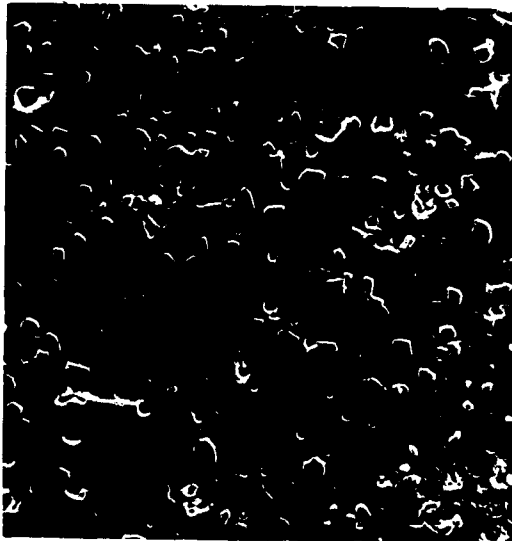


Figure 9a. 1.0 μm \times
Scanning electron micrograph of polished and acid-etched sample with Sr/Ti = 0.900, slow-cooled from 1400°C.



Figure 9b. 1.0 μm \times
Scanning electron micrograph of polished and acid-etched sample with Sr/Ti = 0.900, slow-cooled from 1400°C.

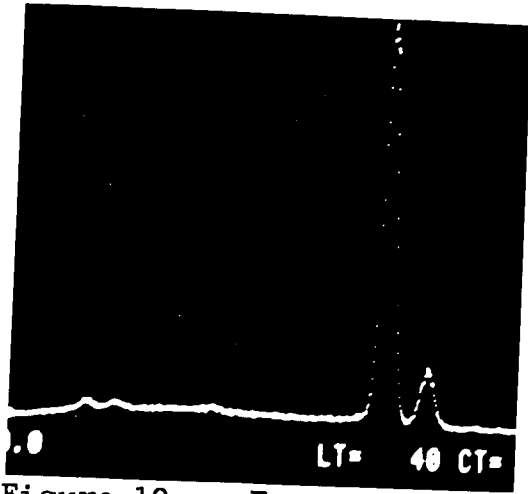


Figure 10a. Energy dispersive spectrum of large second phase particle shown in Figure 9a.

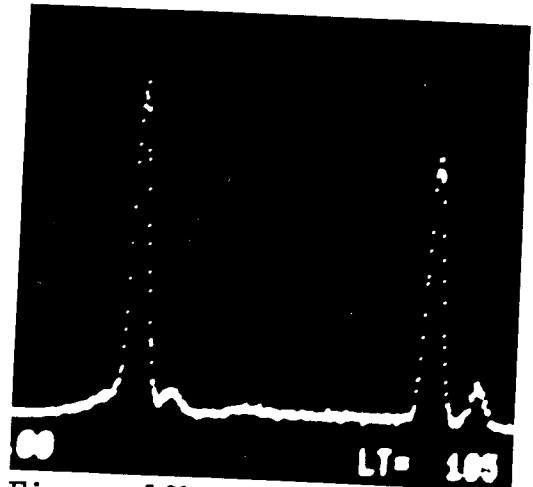


Figure 10b. Energy dispersive spectrum of matrix shown in Figure 9a.

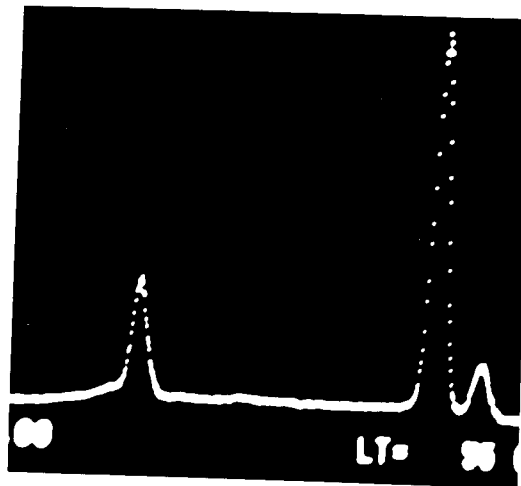


Figure 10c. Energy dispersive spectrum of small second phase particle shown in Figure 9a.

SrO-TiO₂

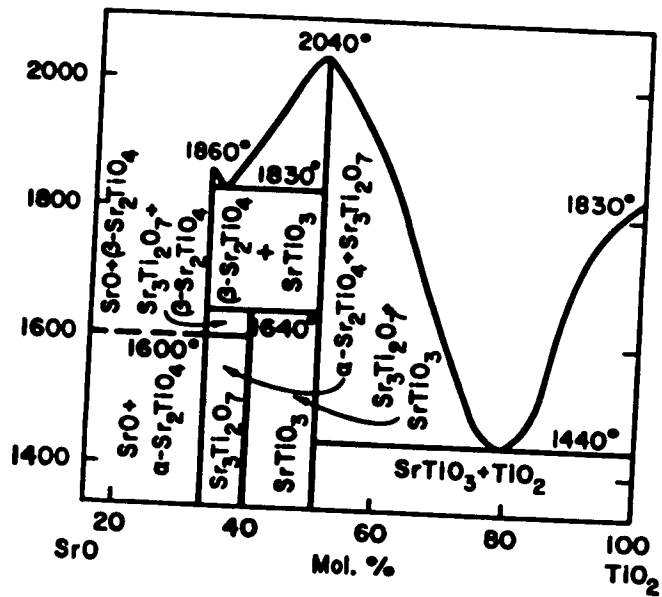


Figure 11. SrO-TiO₂ Phase Diagram (29)



Figure 12a. 1.0 μm H
 Scanning electron micrograph
 of polished and acid-etched
 sample with Sr/Ti = 0.810,
 slow-cooled from 1400°C.



Figure 12b. 1.0 μm H
 Scanning electron micrograph
 of polished and acid-etched
 sample with Sr/Ti = 0.810,
 slow-cooled from 1400°C.

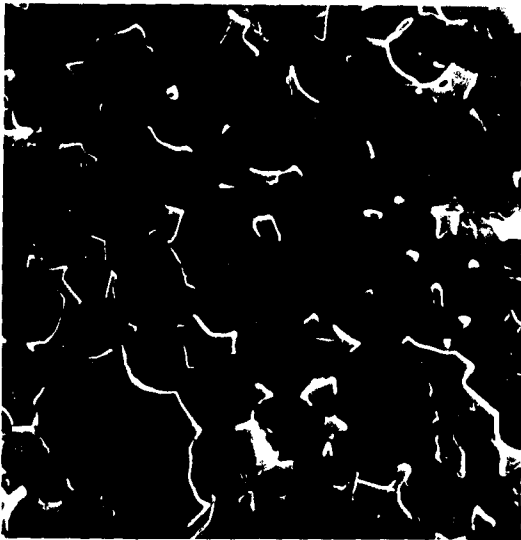


Figure 12c. 1.0 μm H
 Scanning electron micrograph
 of polished and acid-etched
 sample with Sr/Ti = 0.810,
 quenched from 1470°C.

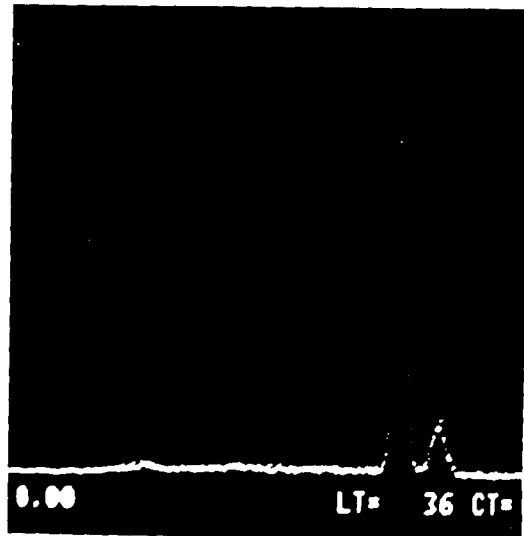


Figure 12d.
 Energy dispersive spectrum
 of large second phase
 particle shown in Fig. 12c.



Figure 13a. 1.0 μm \dashv
Scanning electron micrograph
of polished and acid-etched
sample with Sr/Ti = 0.995,
slow-cooled from 1400°C.

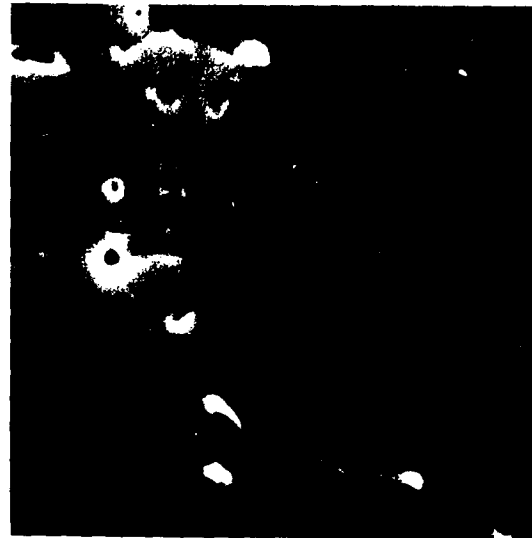


Figure 13b. 1.0 μm \dashv
Scanning electron micrograph
of polished and acid-etched
sample with Sr/Ti = 0.995,
quenched from 1400°C.



Figure 13c. 1.0 μm \dashv
Scanning electron micrograph
of acid-etched "hole" in
sample with Sr/Ti = 0.995,
quenched from 1400°C.

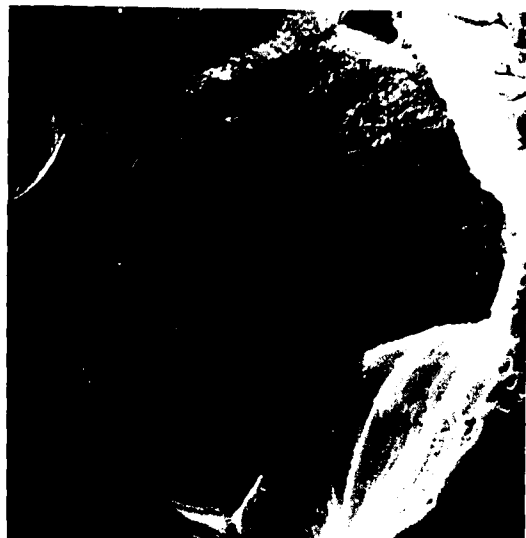


Figure 13d. 1.0 μm \dashv
Scanning electron micrograph
of acid-etched "hole" in
sample with Sr/Ti = 0.995,
quenched from 1470°C.



Figure 14a. 1.0 μm \leftarrow
Scanning electron micrograph of polished
and acid-etched sample with Sr/Ti = 1.000,
slow-cooled from 1400°C.



Figure 14b. 1.0 μm \leftarrow
Scanning electron micrograph of polished
and thermally-etched sample with Sr/Ti =
1.000, slow-cooled from 1400°C

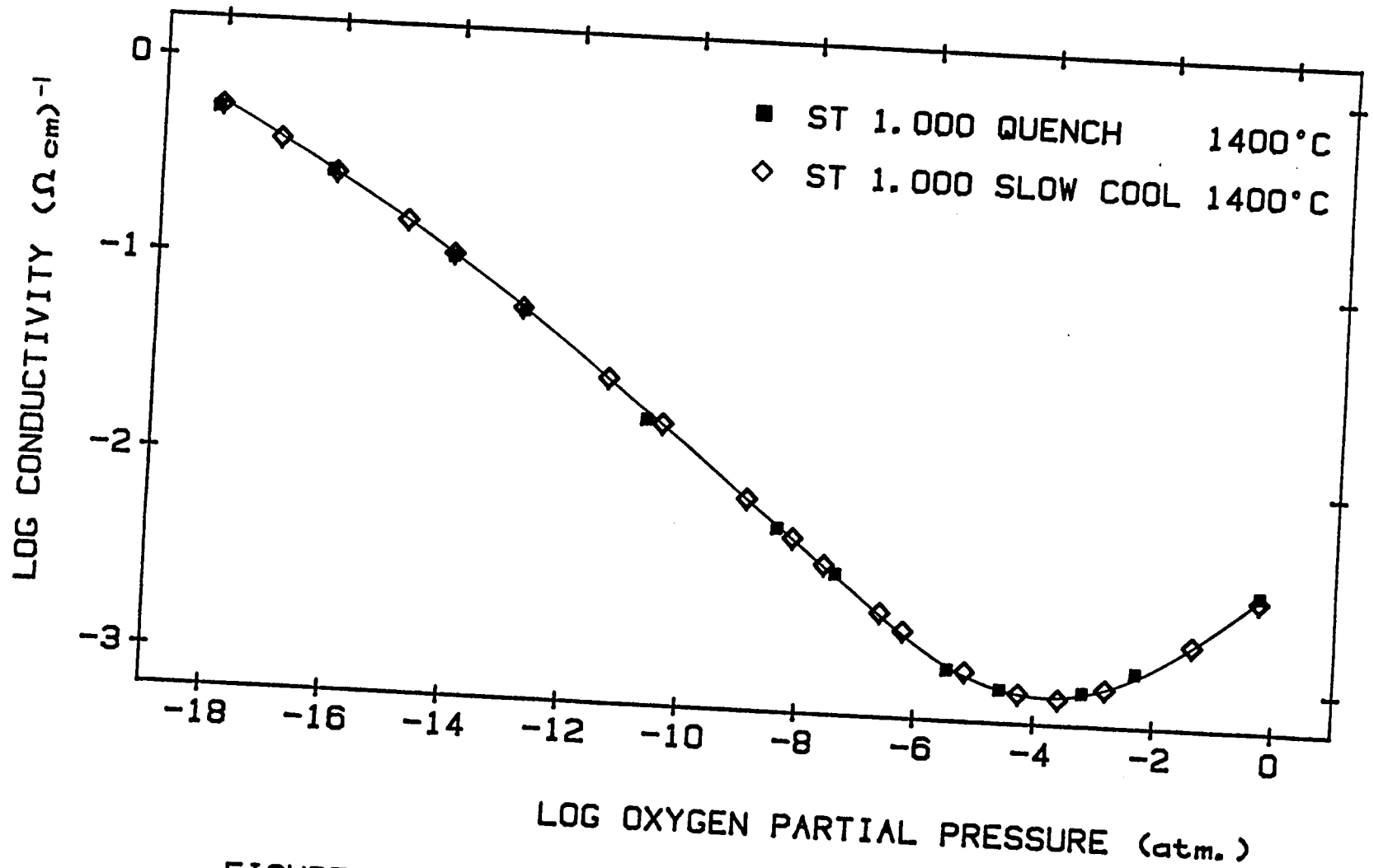


FIGURE 15 : LOG σ vs LOG P_{O_2} FOR UNDOPED $SrTiO_3$

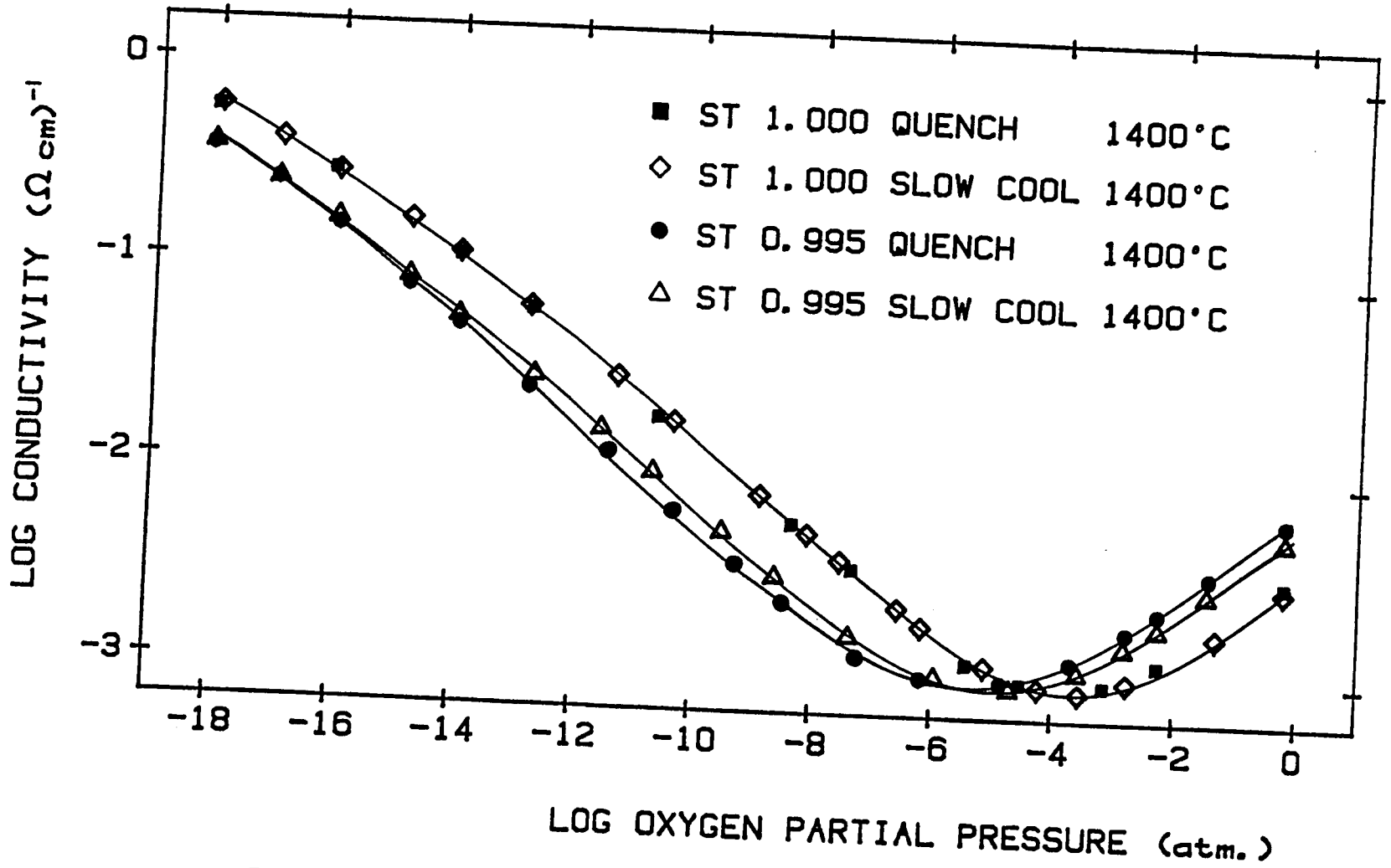


FIGURE 16 : LOG σ vs LOG P_{O_2} FOR UNDOPED $SrTiO_3$

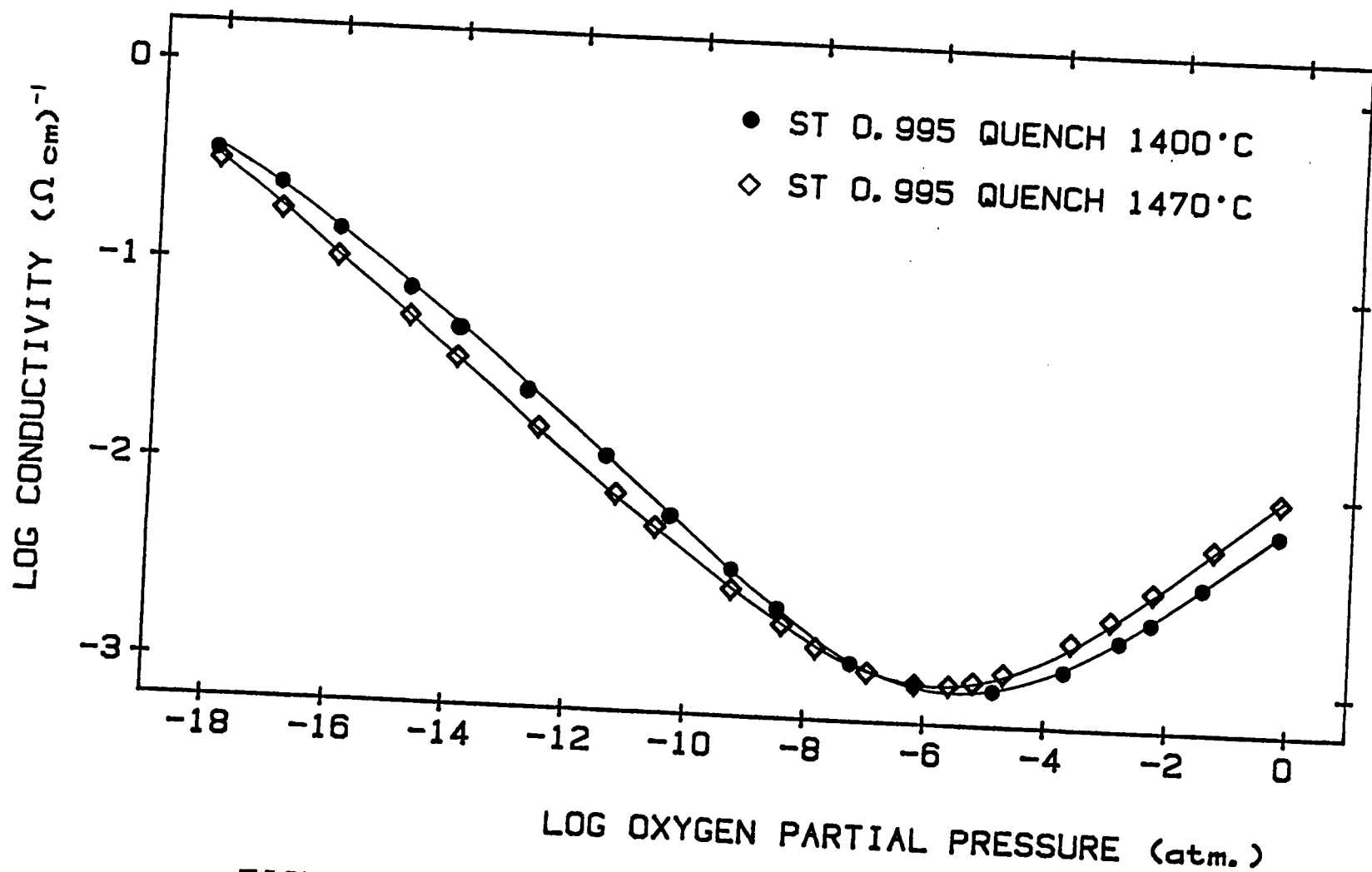
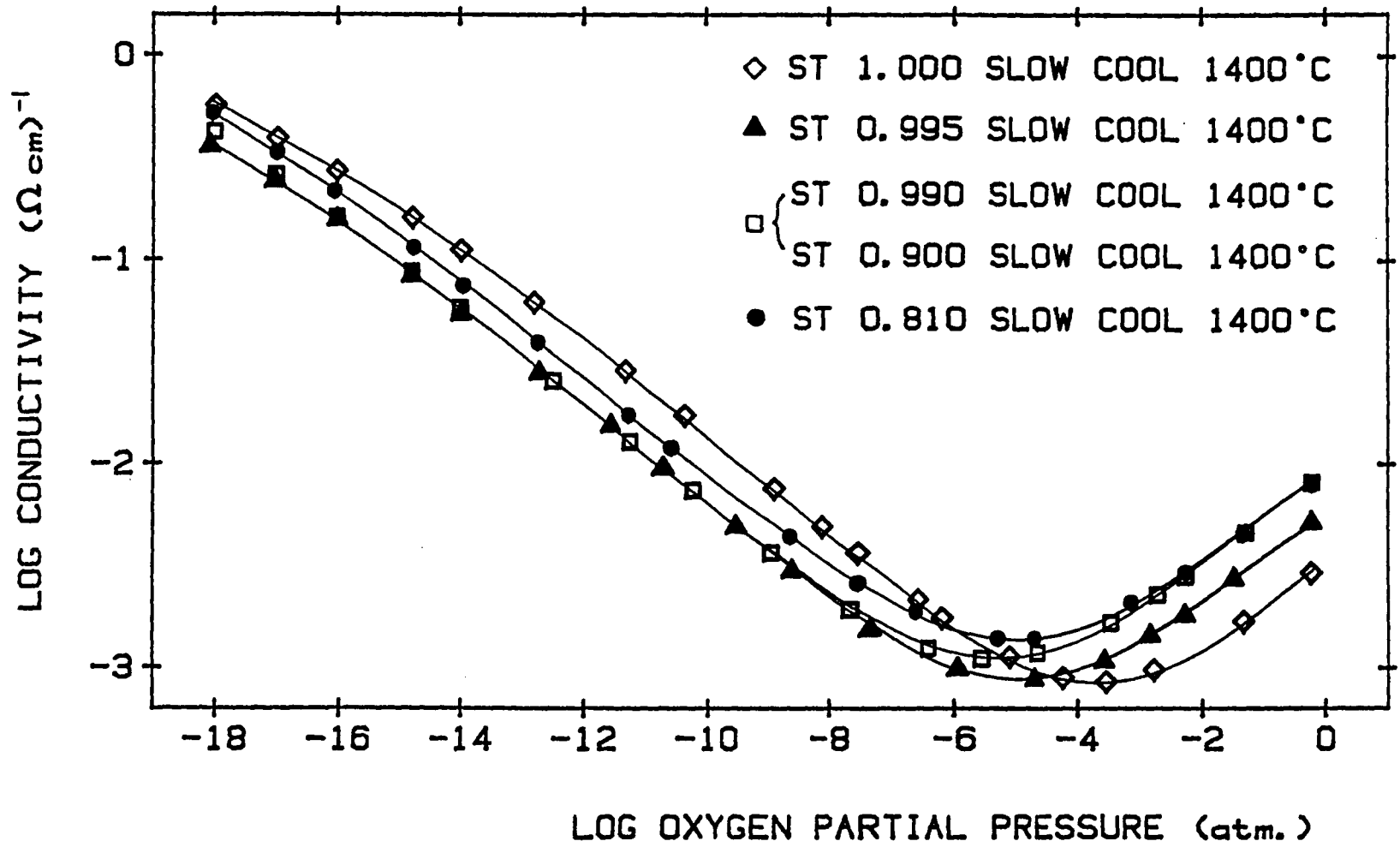


FIGURE 17 : LOG σ vs LOG P_{O_2} FOR UNDOPED SrTiO_3


 FIGURE 18 : LOG σ vs LOG P_{O_2} FOR UNDOPED SrTiO_3

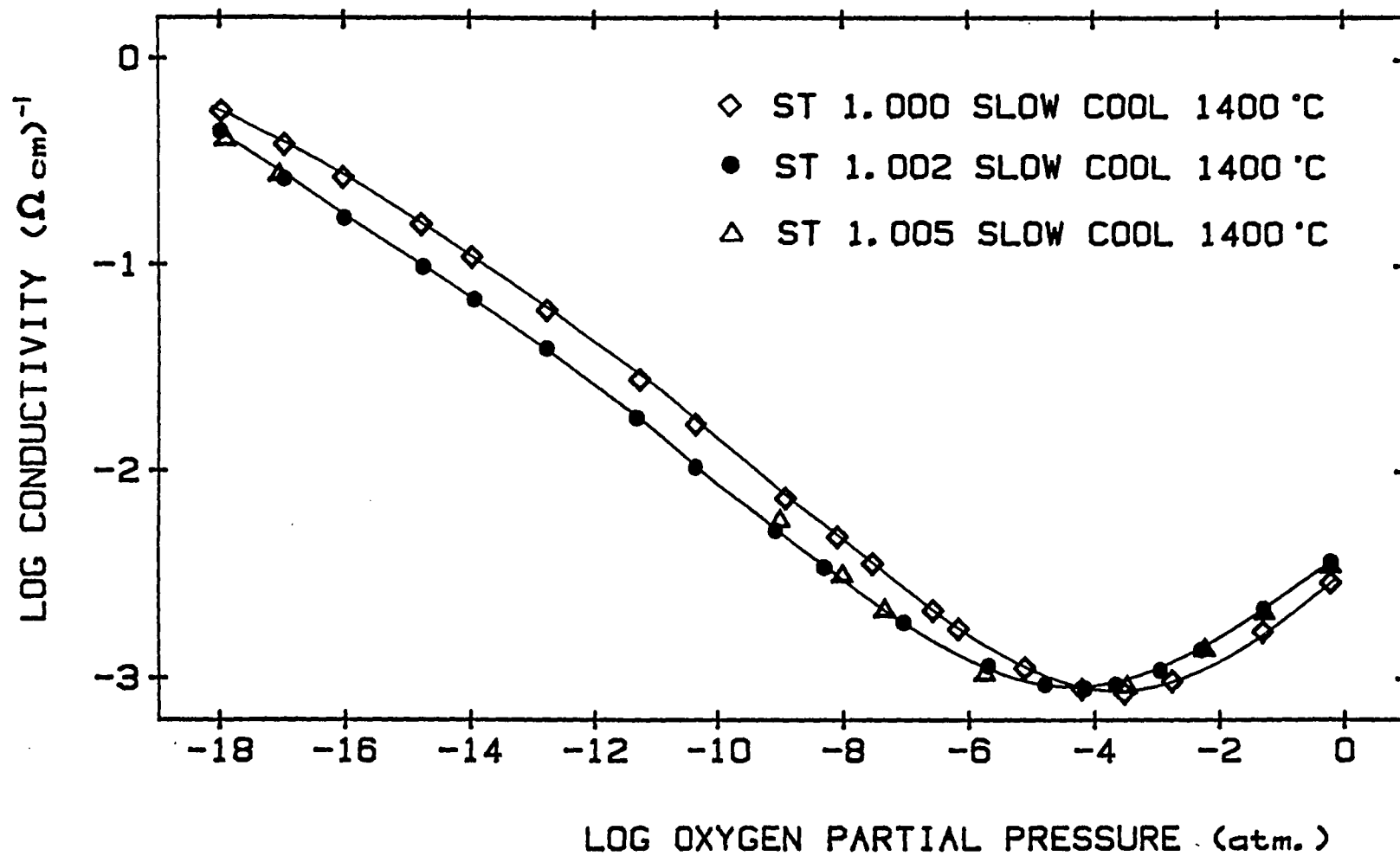


FIGURE 19 : LOG σ vs LOG P_{O_2} FOR UNDOPED SrTiO₃

3.2 Impurity Behaviour in BaTiO₃ and SrTiO₃

Table 1b shows a summary of Lee's results (19) and Table 2 lists the compositions that were investigated as a continuation of his work. All conductivity measurements were made at 1000°C. The conductivity profiles for these samples are shown in Figs. 20-22, and a summary of the observed types of behaviour is given in Table 3, together with Lee's results for comparison.

Figures 20 and 21 are the conductivity profiles obtained for the Al- and Sc-doped SrTiO₃ and the Al-doped BaTiO₃, respectively, with A/B > 1 in all three cases. The curves are very similar to the one shown in Fig. 1 for acceptor-doped SrTiO₃ with A/B ≤ 1, and may be explained using the defect model outlined in the Introduction. From the summary of results in Table 3 it can be seen that BaTiO₃ and SrTiO₃ both exhibit acceptor-type behaviour when doped with Al or Sc, regardless of the Ba/Ti or Sr/Ti ratio. Note that the conductivity profile for the Al-doped SrTiO₃ in Fig. 20 does not include a -1/6 dependence of conductivity in the lowest region of PO₂, whereas there is a limited -1/6 dependence exhibited by the Sc-doped sample. This suggests that the larger concentration of Al is a major source of V_O^{••} even at a PO₂ of 10⁻¹⁸ atm. and dominates over the reduction reaction, which results in the -1/4 dependence of conductivity according to Eq. (9).

Figure 22 includes the conductivity profile obtained for Nb-doped BaTiO₃ with excess BaO, which shows similar behaviour to that of the equivalent SrTiO₃ composition studied by Lee. Both materials exhibit para-donor behaviour. Lee has explained this type of behaviour by dividing the conductivity profile into three regions: Region 1, decrease of log σ at a slope of -1/6; Region 2, the oxygen pressure-independent region; Region 3, decrease of log σ at a slope of -1/8. These are described as follows:

Region 1 -- The reduction reaction, Eq. (1), is the major source of defects. The carrier concentration has the same dependence on the oxygen partial pressure as in Region I of the acceptor-doped or donor-doped material,

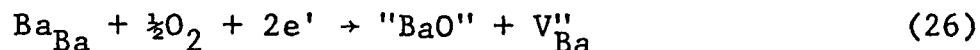
i.e.
$$n = (2K_1)^{1/3} P_{O_2}^{-1/6} \quad (7)$$

Taking logarithms of both sides, a -1/6 dependence of log n (and therefore a -1/6 dependence of log σ) on log P_{O₂} is obtained.

Region 2 -- This mid-P_{O₂} region corresponds to the oxygen pressure-independent region (Region II) of the donor-doped behaviour described in the introduction (Eq. (23)). In the para-donor case this behaviour is only observed in a very limited region of P_{O₂} and a change in slope occurs at higher values of P_{O₂}.

Region 3 -- Lee has proposed that at the higher P_{O₂},

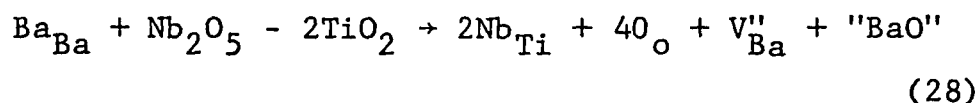
oxygen ions are incorporated into an appropriate crystal site to form "BaO" and leave behind vacant barium sites



There are two possible sites for the incoming oxygen: one is the segregation of excess BaO to form the second phase in the grain boundary; the other is by accommodation in a structural change, such as the formation of an ordered structure with blocks of perovskite BaTiO_3 separated by layers of BaO, which has been proposed by Ruddlesden and Popper (23) in the case of SrTiO_3 and further confirmed by Tilley (24). The barium vacancy, V''_{Ba} , is controlled by the amount of dopant

$$[D^\bullet] \approx 2[V''_{\text{Ba}}] \quad (27)$$

which is the condition of charge neutrality for the following reaction:



Since the mass action expression for Eq. (26) is

$$n^2 \propto [V''_{\text{Ba}}] \text{PO}_2^{-\frac{1}{2}} \quad (29)$$

then the combination of Eqs. (27) and (29) leads to

$$n \propto \text{PO}_2^{-\frac{1}{4}} \quad (30)$$

According to the preceding argument, it is expected that a $-\frac{1}{4}$ dependence of conductivity should be observed in the region of high oxygen partial pressure. However, the results show a $-1/8$ dependence, which may represent

some sort of transition between donor-type (or oxygen pressure-independent) behaviour and acceptor-type (or $-\frac{1}{2}$ dependent) behaviour.

Figure 22 also includes the conductivity profile obtained for La-doped BaTiO_3 with excess BaO , which exhibits a very similar para-donor-type behaviour to the Nb-doped material.

From the summary of results in Table 3, it can be seen that Al- and Sc-doping gives rise to acceptor-type behavior in both SrTiO_3 and BaTiO_3 , regardless of the Sr/Ti or Ba/Ti ratio. It thus appears that these two trivalent dopant cations always occupy the Ti sites. The magnitude of the difference in charge is the same whether the trivalent dopant cation substitutes for a Ti ion or for a Sr (or Ba) ion. However, Al and Sc ions are closer in size to that of a Ti ion (Table 1a) and are therefore expected to occupy Ti sites in the lattice. The Al ion is actually slightly smaller than a Ti ion and will be very unlikely to substitute for the larger Sr or Ba ion in preference to substitution for a Ti ion. Al- or Sc-doping is therefore expected to result in acceptor-type behaviour, and this is found to be the case.

Y is also a trivalent ion, so that its charge should not influence which site it occupies. The size of the Y ion is almost halfway between that of a Ti ion and that of a Ba, so that it seems equally likely that the Y ion

will occupy either site in BaTiO_3 . From the results in Table 3, Y-doping does not always give rise to acceptor-type behaviour. In the case of BaTiO_3 , excess TiO_2 appears to force the Y onto the Ba site to give $\text{Y}_{\text{Ba}}^{\cdot}$ and donor-type behaviour, whereas excess BaO forces the Y ion onto a Ti site to give $\text{Y}_{\text{Ti}}^{\cdot}$ and acceptor-type behaviour. In the case of SrTiO_3 , the Y ion is closer in size to a Sr ion and Y-doping is more likely to give $\text{Y}_{\text{Sr}}^{\cdot}$ and donor-type behaviour even in the presence of excess SrO. Para-donor-type behaviour is actually observed in this case.

The presence of excess TiO_2 in SrTiO_3 results in acceptor-type behaviour in all cases. In other words, the excess TiO_2 appears to be most effective in altering the behaviour of impurities in SrTiO_3 . This may be related to the fact that excess TiO_2 is more soluble in SrTiO_3 than in BaTiO_3 , and also it is more soluble than SrO in SrTiO_3 as reported in section 3.1.

Assuming the Y ion sits on a Sr site, the loss of donor-doped characteristics could be due to the increase in $V_{\text{O}}^{\cdot\cdot}$ content produced by solution of excess TiO_2 (Eq. (2)), where the extra oxygen carried by the donor impurity can be accommodated in the lattice until finally it is all retained and the characteristic donor-type behaviour is no longer observed. This effect is not observed in BaTiO_3 since excess TiO_2 is practically insoluble in BaTiO_3 .

The La ion has a size very close to that of a Sr ion. Again the charge of the La ion is not thought to influence which site it occupies in the lattice since it is a trivalent ion, but from consideration of its relative size it is expected to substitute for a Sr ion rather than a Ti ion. Consequently, donor-type behaviour is predicted for La-doped SrTiO_3 . This is observed in SrTiO_3 with excess SrO, but not in SrTiO_3 with excess TiO_2 . As in the case of Y-doped SrTiO_3 , acceptor-type behaviour is observed for La-doped SrTiO_3 in the presence of excess TiO_2 , and the same explanation holds. In the case of BaTiO_3 , the size of the La ion is intermediate between that of a Ba ion and that of a Ti ion, but from the results in Table 3, it seems to prefer to occupy a Ba site even in the presence of excess BaO.

The Nb ion has a size very close to that of a Ti ion, and a valency of +5, so that it would appear more favorable for a Nb ion to occupy a Ti site as far as both size and charge imbalance are concerned. This would lead to donor-type behaviour, which incidentally would also be observed if the Nb ion occupied a Sr or Ba site. This behaviour is observed in BaTiO_3 with excess TiO_2 . The total loss of donor-type characteristics in SrTiO_3 with excess TiO_2 and the partial loss of donor-type characteristics in SrTiO_3 with excess SrO may be explained by the greater solubility of the excess TiO_2 ,

which therefore produces more oxygen vacancies to help accommodate the extra oxygen carried by Nb_2O_5 according to Eq. (24). The para-donor-type behaviour cannot be easily explained in the case of Nb-doped BaTiO_3 with excess BaO, unless it is assumed that there is also some solubility of excess BaO in BaTiO_3 .

TABLE 1b: Impurity Behavior in BaTiO₃ and SrTiO₃
(Lee's Work)

	Dopant	Behavior	
		BaTiO ₃	SrTiO ₃
TiO ₂ deficient A/B > 1	La ⁺³	-	D
	Y ⁺³	A	(D)
	Sc ⁺³		
	Al ⁺³		
	Nb ⁺⁵		(D)
TiO ₂ excess (or stoichiometric) A/B $\bar{<$ 1	La ⁺³	D	A
	Y ⁺³	D	A
	Sc ⁺³	A	
	Al ⁺³	A	A
	Nb ⁺⁵	D	A

TABLE 2. Samples Investigated as a Continuation of
Lee's Work

	Sample I.D.	A/B Ratio	Dopant Concentration in Mol. PPM	Dopant
SrTiO_3 A/B = Sr/Ti	ST1.005	1.005	1405	Al
	ST1.005	1.005	1132	Sc
BaTiO_3 A/B = Ba/Ti	BT1.005	1.005	1284	Al
	BT1.005	1.005	1124	Nb
	BT1.002	1.002	822	La

All samples were sintered at 1400°C in air.

TABLE 3: Impurity Behavior in BaTiO₃ (*this study)

	Dopant	Behavior	
		BaTiO ₃	SrTiO ₃
TiO ₂ deficient A/B > 1	La ⁺³	(D)*	D
	Y ⁺³	A	(D)
	Sc ⁺³		A*
	Al ⁺³	A*	A*
	Nb ⁺⁵	(D)*	(D)
TiO ₂ excess (or stoichiometric) A/B $\bar{< 1$	La ⁺³	D	A
	Y ⁺³	D	A
	Sc ⁺³	A	
	Al ⁺³	A	A
	Nb ⁺⁵	D	A

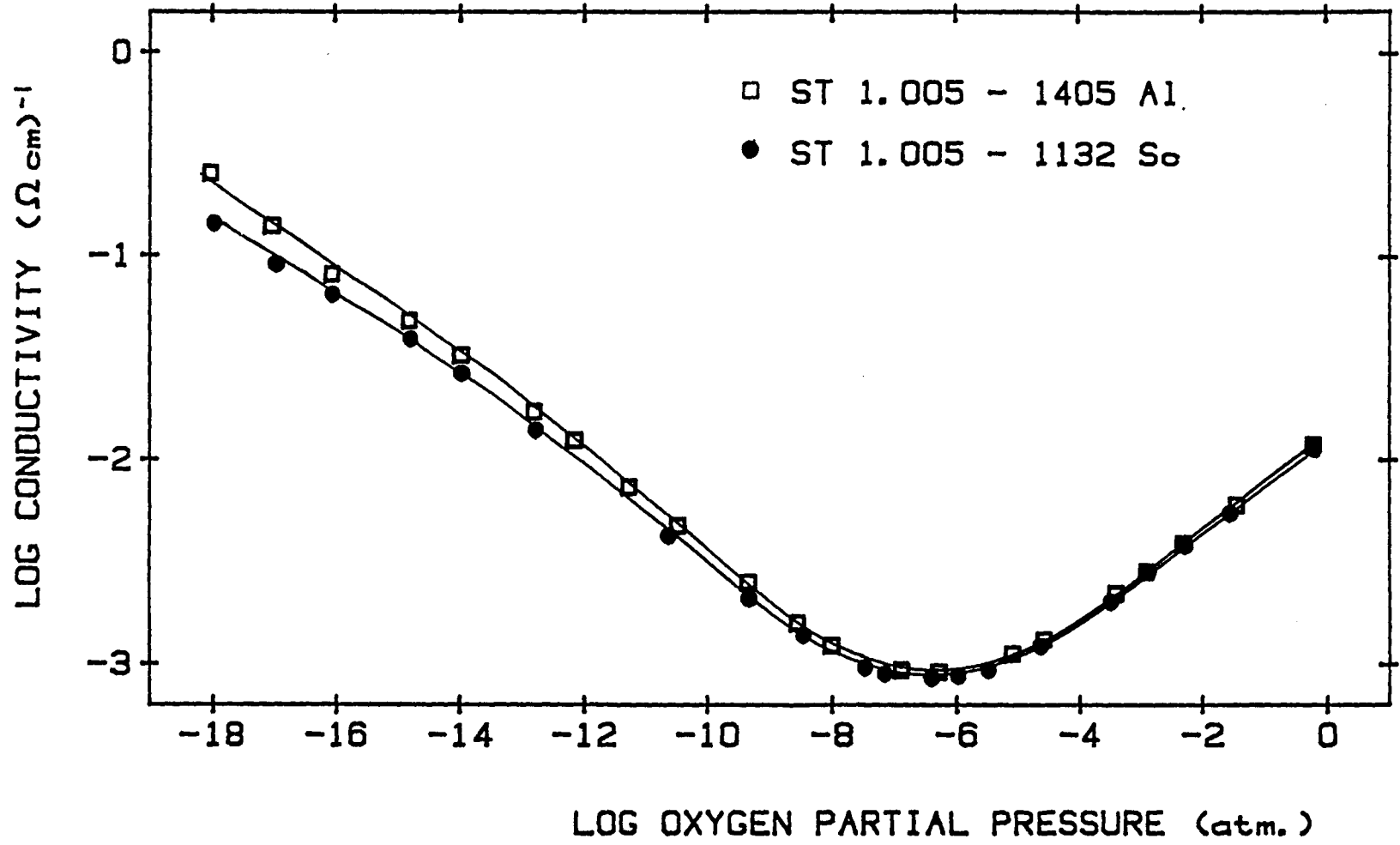


FIGURE 20: LOG σ vs LOG P_{O_2} FOR Al- AND Se-DOPED $\text{SrTi}_{10}\text{O}_3$

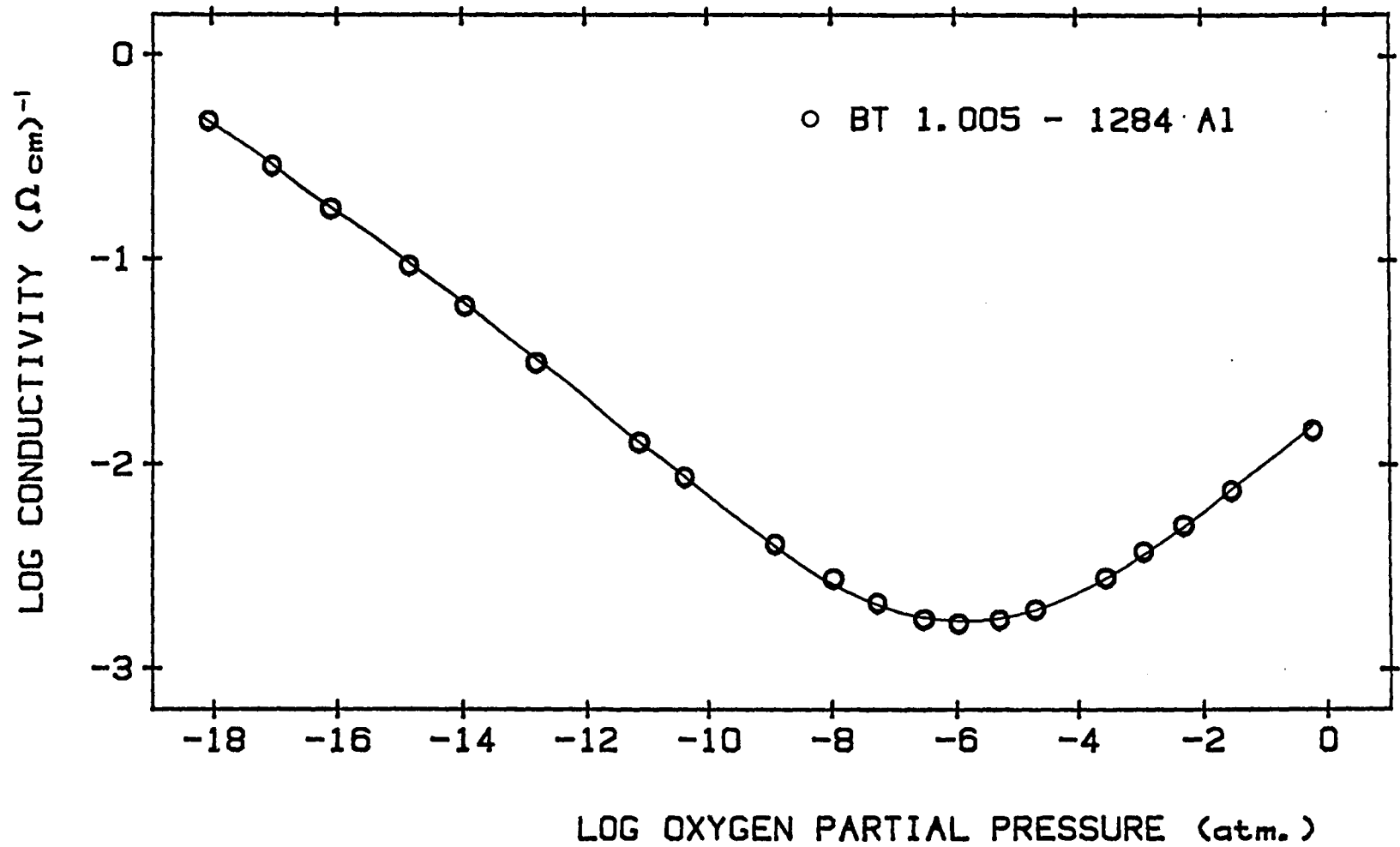


FIGURE 21 : LOG σ vs LOG P_{O_2} FOR Al-DOPED $BaTiO_3$

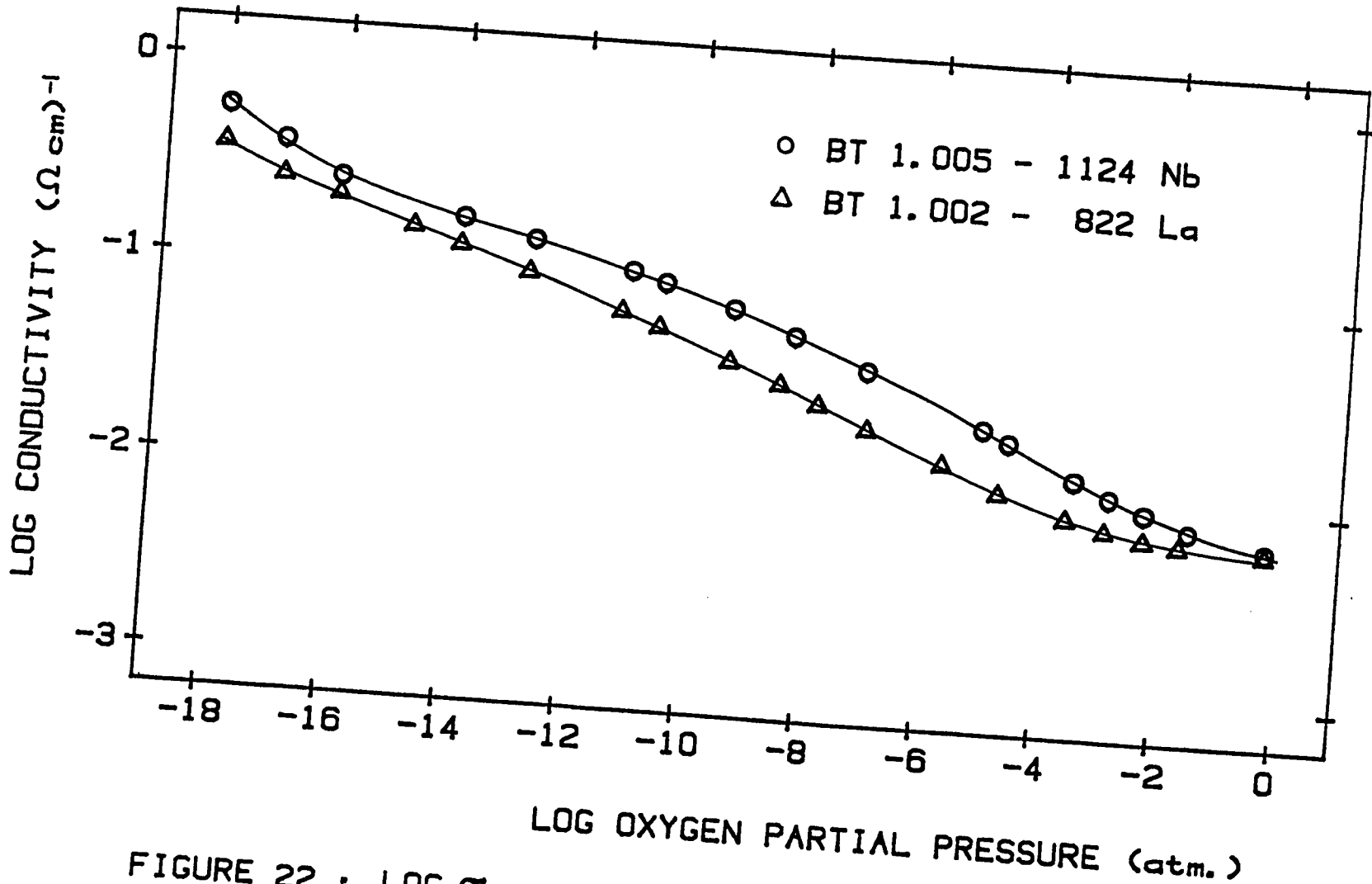


FIGURE 22 : LOG σ vs LOG P_{O_2} FOR Nb- AND La-DOPED $BaTi_{10}O_3$

3.3 The Effect of Al-Doping on the Electrical Conductivity of SrTiO₃ and BaTiO₃

It has been shown in section 3.1 that BaTiO₃ and SrTiO₃ both exhibit acceptor-type behavior when doped with Al, regardless of the Ba/Ti or Sr/Ti ratio. The effect of the added Al, as an acceptor impurity, on the conductivity of BaTiO₃ or SrTiO₃, is consistent with the defect model described in the Introduction. Al-doping produces a shift in the conductivity minimum as predicted by Eq. (18). This can be seen in our results, in the case of SrTiO₃ with Sr/Ti = 1.005, by comparing Fig. 9 and Fig. 22 which show the conductivity profiles for Al-doped SrTiO₃ and undoped SrTiO₃, respectively.

The effect of larger amounts of Al on the conductivity of SrTiO₃ and BaTiO₃ has been investigated in this study. Figure 23 compares conductivity profiles obtained for two 10,000 ppm Al-doped SrTiO₃ samples with the profile shown in Fig. 9 which represents an Al-dopant concentration of 1405 ppm. A shift in the conductivity minimum to lower PO₂ is observed for the two highly-doped materials, with a slightly further shift in the one containing excess SrO. (The excess Sr may force more Al dopant ions onto Ti sites, which would result in a higher concentration of V_O^{••} ext and explain the observed further shift in the minimum to lower PO₂.) The shape

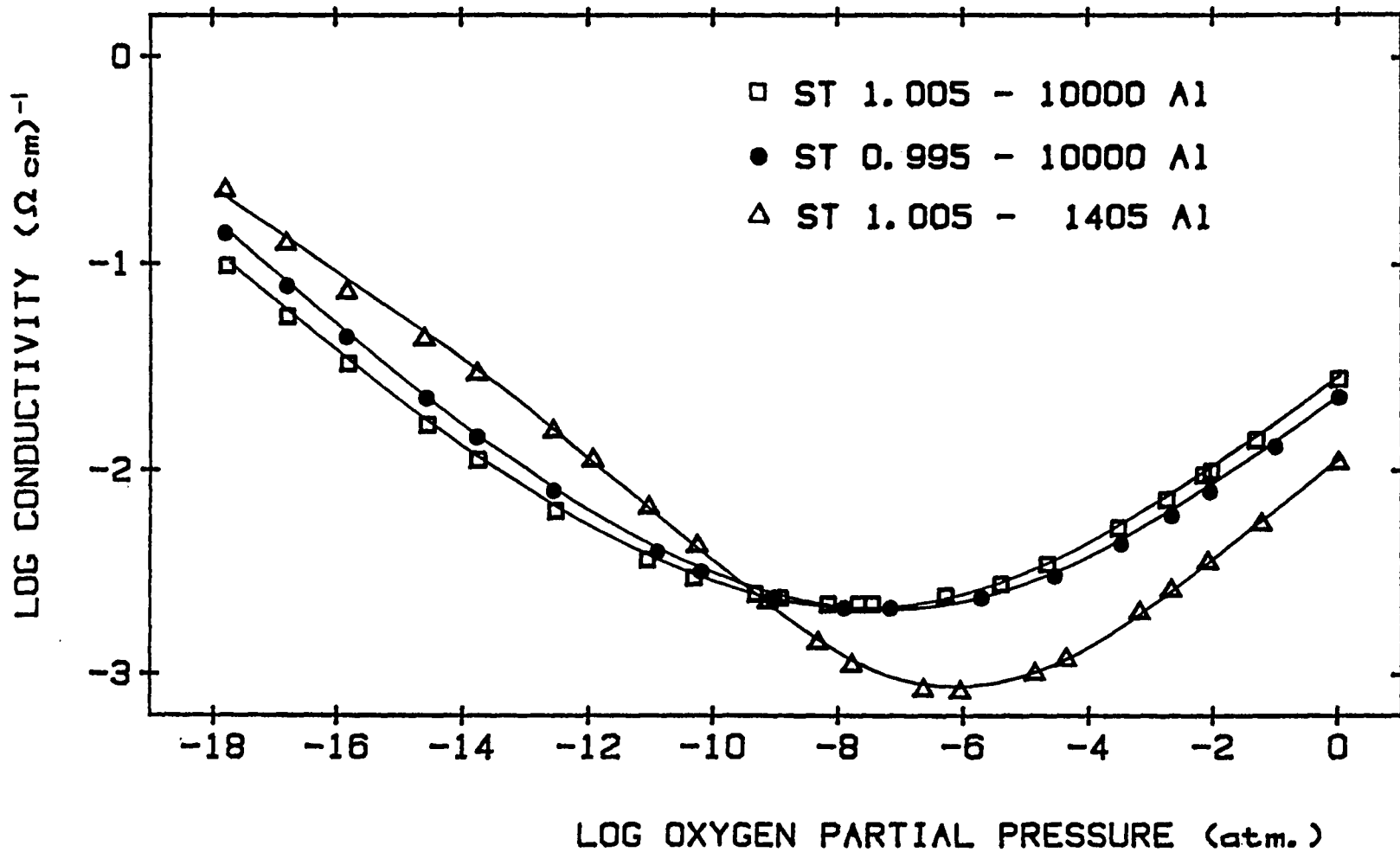
of the conductivity minimum has also changed, and is now flatter in the case of the highly-doped samples.

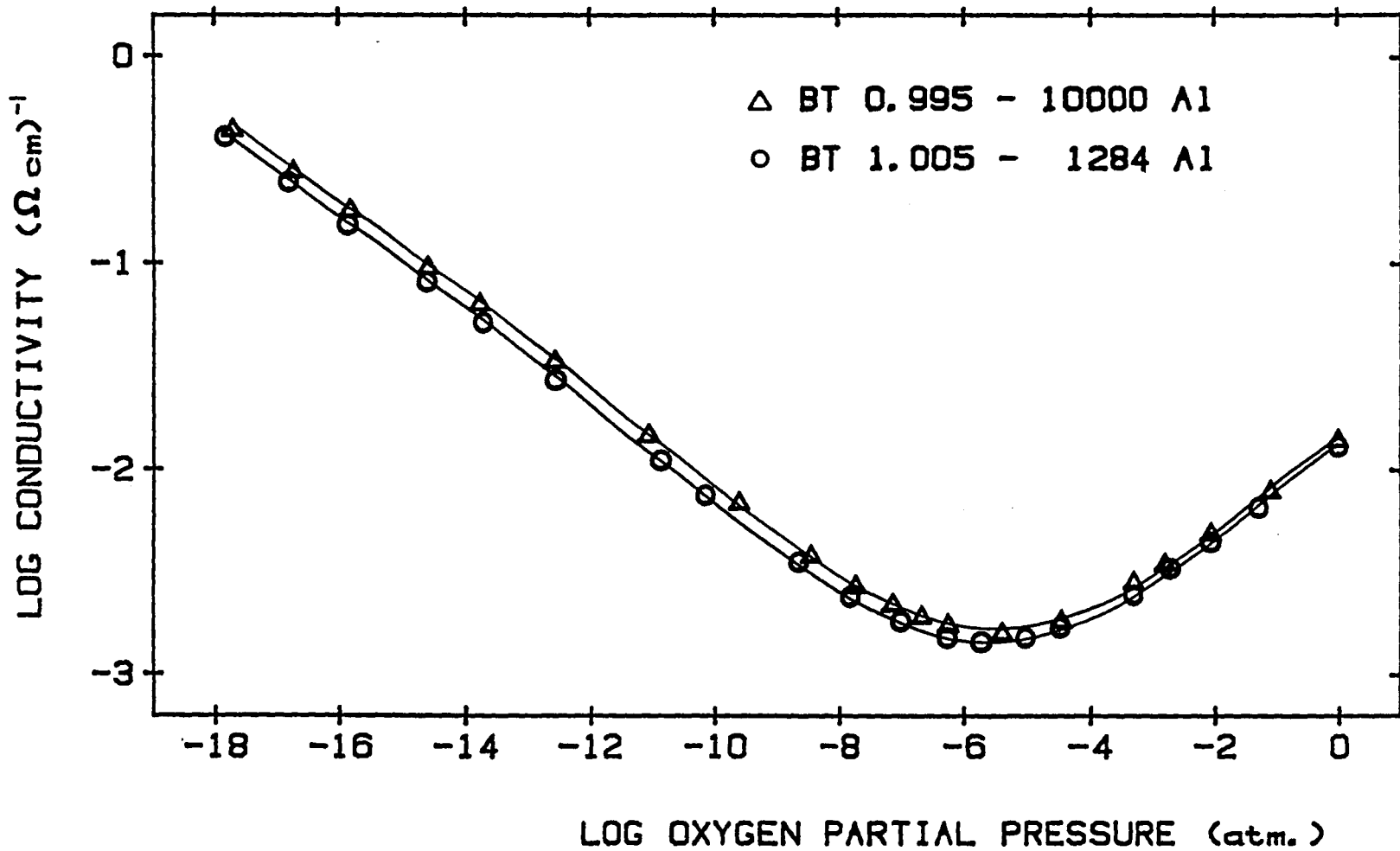
Figure 24 compares the conductivity profiles of BaTiO_3 containing 10,000 ppm Al and 1284 ppm Al, and shows no further shift in the minimum.

As explained in the Introduction, the shift serves as a measure of the relative extrinsic V_{O}'' content, which is increased by the solution of Al in the titanate sublattice according to Eq. (3). Thus it appears from the above results that Al is more soluble in SrTiO_3 than in BaTiO_3 . This suggests that the A-site ions (Sr or Ba) play a role in determining whether or not the Al ion occupies a Ti site according to the reaction described by Eq. (3).

The Al seems to be slightly more soluble in the SrTiO_3 when $\text{Sr/Ti} > 1$. It is believed that excess SrO produces fewer V_{O}'' ext than excess TiO_2 (see section 3.2) and will therefore be less likely to reduce the solubility of the Al.

It has been proposed (10) that the nonideal shape of the conductivity minima is due to a conductivity contribution that is essentially independent of PO_2 and is so small that it affects the results only near the minima. It is suggested that this is due to conduction by extrinsic V_{O}'' , which becomes more significant at higher Al-dopant concentrations in SrTiO_3 .

FIGURE 23 ; LOG σ vs LOG P_{O_2} FOR Al-DOPED SrTiO₃

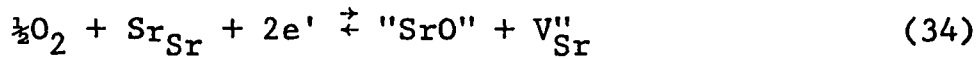
FIGURE 24 : LOG σ vs LOG P_{O_2} FOR Al-DOPED BaTiO₃

3.4 The Effect of Nb-Doping on the Electrical Conductivity and Microstructure of SrTiO₃

Figure 25 shows the conductivity profiles obtained for Nb-doped SrTiO₃ compositions with Sr/(Ti+Nb) = 0.995. (The samples had been slow-cooled from a sintering temperature of 1400°C.) Acceptor-type behaviour is observed in the material doped with 2,000 ppm Nb. The samples containing 5,000 ppm and 10,000 ppm Nb exhibit donor-type behaviour, with the PO₂-independent region extending to lower oxygen pressures for the more highly-doped material. As the Nb-dopant concentration is increased further to 15,000, 20,000 and 30,000 ppm, an acceptor-type PO₂-dependence of conductivity with a - $\frac{1}{2}$ slope is observed at intermediate oxygen pressures. These highly-doped samples differ from the 2,000 ppm Nb-doped acceptor-type material in that their conductivity profiles do not include a minimum, with the - $\frac{1}{2}$ dependence extending to an oxygen pressure of 1 atmosphere.

The defect models explaining the acceptor- and donor-type behaviour have been described in the Introduction. The model used in section 3.1 to explain para-donor type behaviour may be applied to the results obtained here for the highly-doped materials, where at intermediate and higher oxygen pressures the donor-type characteristics are lost. In effect, the material takes up exactly enough oxygen to absorb all of the impurity-related electrons

as the oxygen is transformed into oxide ions. With the loss of extrinsic electrons, some other negatively charged defect must appear to balance the positive charges of the donor centers. Since interstitial oxide ions are unlikely in the perovskite structure, it has been proposed that the added oxygen combines with strontium extracted from the SrTiO_3 to form a Sr-rich second phase, leaving strontium vacancies, V''_{Sr} , in the crystalline bulk to compensate the donors



"SrO" represents a Sr-rich second phase, analogous to the "BaO" described in Eq. (28) for BaTiO_3 , in which case the following dependence was derived.

$$n \propto \text{PO}_2^{-\frac{1}{4}} \quad (30)$$

This dependence is observed in the profiles for the highly-doped SrTiO_3 samples shown in Fig. 25.

Daniels and Härdtl (11) have also observed this $-\frac{1}{4}$ dependence of $\log \sigma$ on $\log \text{PO}_2$ for highly La-doped BaTiO_3 and suggest that the La donors are predominantly compensated by doubly ionized metal vacancies. Gravimetric measurements by Eror and Smyth (13) on donor-doped BaTiO_3 have shown that the reversible change of oxygen content, between specified states of oxidation and reduction, is proportional to the dopant concentration. The driving force for additional uptake of oxygen is the compensation of the electronic disorder introduced by

the donor-dopant. The increase in energy that is required to introduce an ion into the host lattice is more than compensated by the decrease in electronic disorder. The fact that highly donor-doped BaTiO_3 is nonconducting can be explained by this mechanism of "stoichiometric compensation," and it appears from our results that the same may apply to highly donor-doped SrTiO_3 .

Figures 26-30 are scanning electron micrographs of the Nb-doped samples. The grain size is much smaller in the samples containing $\geq 15,000$ ppm Nb, which could be explained by the presence of a grain-growth inhibiting second phase such as "SrO." A second phase was actually observed in the samples containing $\geq 15,000$ ppm Nb, as illustrated in Figs. 29 and 30, although it was impossible to determine the composition of this phase due to its very small width. The microstructures were found to be the same for the two materials doped with 20,000 ppm and 30,000 ppm Nb, and the conductivity profiles for these two samples shown in Fig. 25 are identical. This suggests that their structures are saturated with Nb ions and compensating strontium vacancies, and no more second phase is produced.

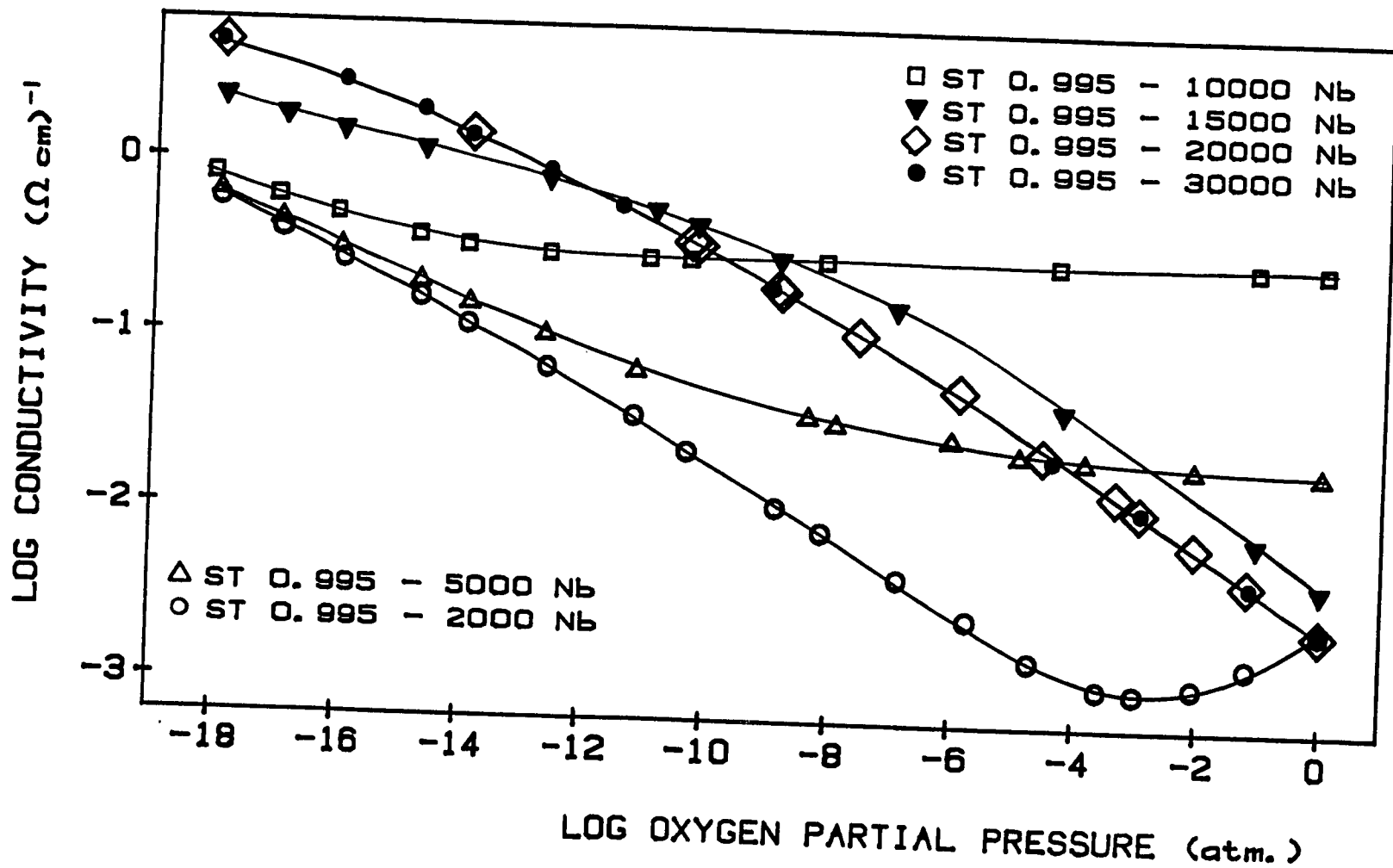


FIGURE 25 : LOG σ vs LOG P_{O_2} FOR Nb-DOPED SrTiO_3




Figure 26. 1.0 μm 
Scanning electron micrograph of acid-etched "hole" in sample with $\text{Sr}/(\text{Ti}+\text{Nb}) = 0.995$, doped with 2000 ppm Nb.




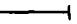
Figure 27. 1.0 μm 
Scanning electron micrograph of acid-etched "hole" in sample with $\text{Sr}/(\text{Ti}+\text{Nb}) = 0.995$, doped with 5000 ppm Nb.



Figure 28. 1.0 μm 
Scanning electron micrograph of acid-etched "hole" in sample with $\text{Sr}/(\text{Ti}+\text{Nb}) = 0.995$, doped with 10000 ppm Nb.

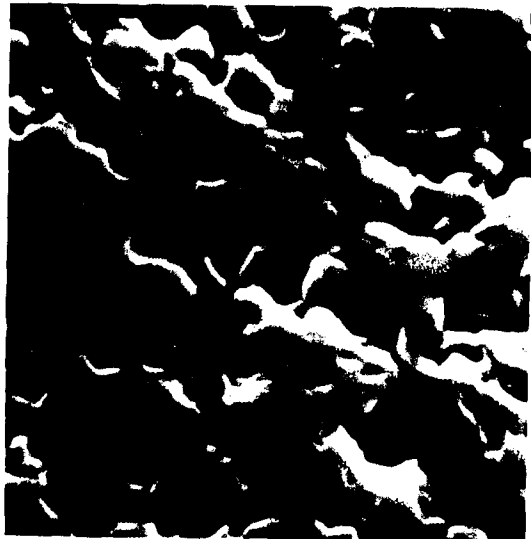



Figure 29. 1.0 μm 
Scanning electron micrograph of polished and acid-etched sample with $\text{Sr}/(\text{Ti}+\text{Nb}) = 0.995$, doped with 15000 ppm Nb.

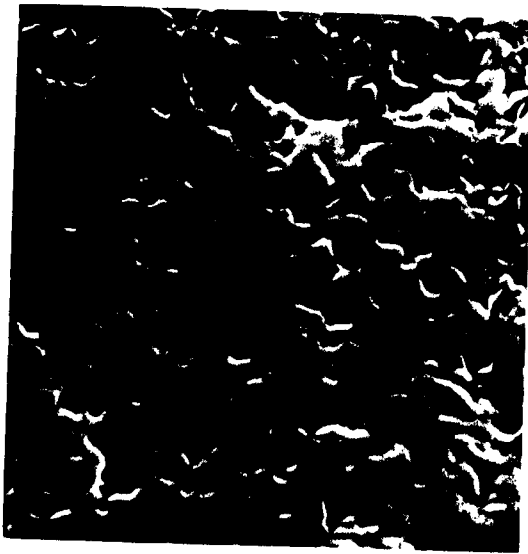
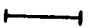


Figure 30. Scanning electron micrograph of polished and acid-etched sample with $\text{Sr}/(\text{Ti}+\text{Nb}) = 0.995$. doped with 20000 ppm Nb.

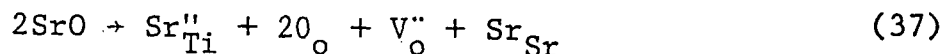
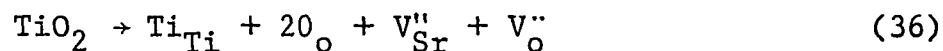
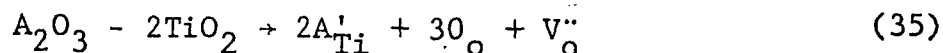
1.0 μm 

CHAPTER IV

CONCLUSIONS

Summary of the discussion leads to the following conclusions:

1. $V_{\text{O}}^{\prime\prime}$ may be introduced into the SrTiO_3 structure by dissolving excess TiO_2 or excess SrO , as well as by acceptor-type doping. The solubility of these various additives differs and therefore the negatively charged defect produced in each case could govern the solubility. The following reactions have been proposed, which account for the changes observed in the conductivity profiles:



The solution of excess SrO (Eq. (37)) produces relatively unfavorable $\text{Sr}_{\text{Ti}}^{\prime\prime}$, and SrO has least solubility. The shift in the conductivity minimum is largest in the case of acceptor-type doping, indicating a higher concentration of $V_{\text{O}}^{\prime\prime}$ and therefore a higher concentration of $\text{A}_{\text{Ti}}^{\prime}$. The lower effective negative charge of this defect and the relatively similar ionic sizes of the acceptor-type dopant ion and the Ti ion may be the reason for the higher solubility of acceptor-type dopants in SrTiO_3 .

2. The solubility of excess TiO_2 in SrTiO_3 increases with temperature, and more of the TiO_2 may be retained in solution by rapidly cooling. Therefore the concentration of V_{O}'' within the material will depend on the cooling rate.

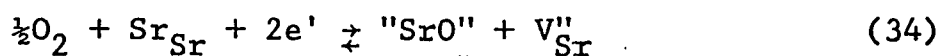
The solubility of excess TiO_2 is greater in SrTiO_3 than in BaTiO_3 , suggesting that either V_{Sr}'' is a more favorable defect than V_{Ba}'' , or that the Ba ions render the accommodation of extra Ti ions more difficult in the same way as they appear to influence the occupation of Ti sites by Al ions (since Al is also more soluble in SrTiO_3 than in BaTiO_3).

3. The Ba/Ti and Sr/Ti ratios play a major role in the impurity behaviour of BaTiO_3 and SrTiO_3 , respectively. In the case of BaTiO_3 , Y impurity ions appear to be forced onto Ti sites by excess Ba to give Y_{Ti}' and acceptor-type behaviour, or onto Ba sites by excess Ti to give Y_{Ba}^{\bullet} and donor-type behaviour, and this is probably due to the fact that the size of the Y ion is midway between the size of the Ba ion and that of the Ti ion. These trends are also observed for La-doped BaTiO_3 , although donor-doped characteristics are not totally lost in the presence of excess Ba, probably because the La ion is larger than the Y ion and will not be forced as easily onto a Ti site.

The solubility of excess TiO_2 in SrTiO_3 , and to a lesser extent the solubility of excess SrO in SrTiO_3 ,

accounts for an increase in V_{O}'' . This helps accommodate the extra oxygen carried by donor-type impurities, (i.e. those with a valency greater than the host cations which they replace). This results in a partial or total loss of donor-type behaviour which gives para-donor-type or acceptor-type behaviour, respectively. In the case of SrTiO_3 , the donor type behaviour expected from Nb-, La-, and Y-doping is not observed at all in the presence of excess TiO_2 , and para-donor behaviour is exhibited by Nb- and Y-doped SrTiO_3 with excess SrO. Excess TiO_2 is more soluble in SrTiO_3 and therefore a greater source of V_{O}'' than SrO, and is more effective in changing the impurity behaviour of SrTiO_3 .

4. Depending on the level of doping, Nb produces strikingly different behaviour in SrTiO_3 containing excess TiO_2 . Low concentrations of Nb are insufficient to overcome the effect of the excess TiO_2 , but as the concentration is increased donor-type behaviour is observed. Further additions of Nb decrease the grain size of the material which is consistent with the appearance of another phase in the grain boundaries. The second phase is believed to be Sr-rich "SrO," formed according to the following reaction:



V_{Sr}'' compensates the donors ($\text{Nb}_{\text{Ti}}^\bullet$), and the donor-type

behaviour is lost so that the material is insulating
when sintered in air.

BIBLIOGRAPHY

1. N. Yamaoka and T. Matsui. *Advances in Ceramics*, Vol. I, p. 232, American Ceramic Society Publication (1981) (Ed. L. M. Levinson).
2. R. Wernicke, *ibid.*, 1, 261 (1981).
3. J. Klerk and P. J. H. Sanders, *ibid.*, 1, 282 (1981).
4. H. Yamada and G. R. Miller, *J. Solid State Chem.* 6, 169 (1973).
5. J. Blanc and D. L. Staebler, *Phys. Rev. B* 4 3548 (1971).
6. L. C. Walters and R. E. Grace, *J. Phys. Chem. Solids*, 28, 239 (1967).
7. A. Yamaji, *J. Amer. Ceram. Soc.* 58 (3-4) 152 (Discussions and Notes) (1975).
8. D. M. Smyth, "Degradation Mechanisms in Ceramic Dielectrics," proposal submitted to U.S. Navy.
9. N.-H. Chan, R. K. Sharma, and D. M. Smyth, *J. Am. Ceram. Soc.* 64 (9) 556 (Sept. 1981).
10. N.-H. Chan, R. K. Sharma, and D. M. Smyth, *J. Am. Ceram. Soc.* 65 (3) 167 (Mar. 1982).
11. J. Daniels, K. H. Härdtl, D. Hennings, and R. Werincke, *Philips Res. Repts.* 31, 487 (1976).
12. A. M. J. H. Seuter, *Philips Res. Rep., Suppl.* 3 (1974).
13. N. G. Eror and D. M. Smyth, "The Chemistry of Extended Defects in Nonmetallic Solids" (L. Eyring, M. O'Keefe, Ed.) North-Holland, Amsterdam (1970) p. 62.
14. N. G. Eror and D. M. Smyth, *J. Solid State Chem.* 24, 235 (1978).
15. S. A. Long and R. N. Blumenthal, *J. Am. Ceram Soc.* 54(10), 515 (Oct. 1971).
16. S. A. Long and R. N. Blumenthal, *J. Am. Ceram. Soc.* 54 (11) 577 (Nov. 1971).

17. N.-H. Chan, R. K. Sharma, and D. M. Smyth, J. of Electrochem. Soc., Vol. 128, No. 8, 1762 (Aug. 1981).
18. F. A. Kröger and H. J. Vink, in "Solid State Physics," Vol. 3 (F. Seitz and D. Turnbull, Ed.) Academic Press, New York (1956).
19. R. Y-F. Lee, Master of Science Thesis, Lehigh University (1981).
20. M. Pechini, "Method of Preparing Lead and Alkaline Earth Titanates and Niobates and Coatings Using the Same to Form a Capacitor," U.S. Pat. 3 330 697, July 11, 1967.
21. R. N. Blumenthal and M. A. Seitz, "Electrical Conductivity in Ceramics and Glass," Part A (N. M. Tallan, Ed.) Chap. 2, p. 107, Marcel Dekker, Inc., New York (1974).
22. R. K. Sharma, N.-H. Chan, and D. M. Smyth, J. Am. Ceram. Soc. 64 (8) 448 (Aug. 1981).
23. S. N. Ruddlesden and P. Popper, Acta Cryst. 11, 54 (1958).
24. R. J. D. Tilley, J. of Solid St. Chem. 21, 293 (1977).
25. N. G. Eror and U. Balachandran, J. of Solid State Chem., 42 (3) 227 (May 1982).
26. O. Mueller and R. Roy, "The Major Ternary Structural Families," Springer, New York (1974).
27. N. Stenton and M. P. Harmer, Advances in Ceramics, Vol. 5, American Ceramic Society Publication (in press).
28. F. S. Galasso, "Structure, Properties and Preparation of Perovskite-type Compounds" (p. 37) Pergamon Press, 1969.
29. E. M. Levin, C. R. Robbins and H. F. McMurdie, "Phase Diagrams for Ceramists," American Ceramic Society Publication (1964).

APPENDIX

The Conductivity Data for all compositions used in this study.

All samples were slow-cooled from a sintering temperature of 1400°C and measured at 1000°C unless otherwise stated.

TABLE 4: The Conductivity Data for ST 1.005-1405 Al.

<u>-log PO₂ (atm.)</u>	<u>log σ(Ωcm)⁻¹</u>
0	-1.92
1.25	-2.22
2.10	-2.41
2.70	-2.55
3.20	-2.66
4.40	-2.89
4.90	-2.96
6.10	-3.05
6.70	-3.04
7.85	-2.92
8.40	-2.81
9.20	-2.61
10.35	-2.33
11.15	-2.14
12.05	-1.91
12.70	-1.77
13.90	-1.49
14.75	-1.32
16.00	-1.09
17.00	-0.85
18.00	-0.59

TABLE 5: The Conductivity Data for ST 1.005-1132 Sc

<u>-log P_{O₂} (atm.)</u>	<u>log σ(Ωcm)⁻¹</u>
0	-1.94
1.35	-2.26
2.06	-2.42
2.66	-2.55
3.28	-2.70
4.45	-2.92
5.29	-3.-4
5.79	-3.07
6.21	-3.08
6.98	-3.06
7.31	-3.03
8.30	-2.87
9.19	-2.69
10.50	-2.38
12.67	-1.86
13.89	-1.58
14.73	-1.41
15.99	-1.19
16.93	-1.04
17.94	-0.84

TABLE 6: The Conductivity Data for BT 1.005-1284 A1

<u>-Log PO₂ (atm.)</u>	<u>Log σ(Ωcm)⁻¹</u>
0	-1.82
1.29	-2.12
2.08	-2.29
2.72	-2.42
3.34	-2.55
4.49	-2.71
5.07	-2.76
5.77	-2.78
6.31	-2.76
7.09	-2.68
7.88	-2.56
8.76	-2.39
10.25	-1.89
10.98	-1.89
12.68	-1.50
13.86	-1.22
14.75	-1.02
16.03	-0.74
17.00	-0.53
18.02	-0.31

TABLE 7: The Conductivity Data for BT 1.005-1124 Nb

<u>-Log PO₂ (atm.)</u>	<u>Log σ(Ωcm)⁻¹</u>
0	-2.19
1.31	-2.11
2.05	-2.03
2.66	-1.96
3.28	-1.88
4.43	-1.71
4.88	-1.65
6.91	-1.39
8.16	-1.24
9.22	-1.12
10.41	-1.01
10.98	-0.96
12.66	-0.83
13.88	-0.74
16.00	-0.57
16.98	-0.40
17.97	-0.24

TABLE 8: The Conductivity Data for BT 1.002-822 La

<u>-Log PO₂ (atm.)</u>	<u>Log σ(Ωcm)⁻¹</u>
0	-2.21
1.46	-2.19
2.04	-2.17
2.71	-2.13
3.38	-2.08
4.56	-1.97
5.56	-1.84
6.86	-1.69
7.71	-1.58
8.37	-1.49
9.25	-1.39
10.48	-1.24
11.12	-1.17
12.73	-1.00
13.91	-0.88
14.73	-0.80
16.01	-0.66
16.97	-0.58
18.00	-0.43

TABLE 9: The Conductivity Data for Undoped ST1.000.
 Quenched from a Sintering Temperature of
 1400°C.

<u>-Log PO₂ (atm.)</u>	<u>Log σ(Ωcm)⁻¹</u>
0	-2.48
2.05	-2.90
2.93	-3.01
4.33	-3.01
5.24	-2.92
7.20	-2.46
8.23	-2.24
10.52	-1.72
12.66	-1.19
13.90	-0.93
16.04	-0.52
18.02	-0.22

TABLE 10: The Conductivity Data for Undoped ST1.000.

<u>-Log PO₂ (atm.)</u>	<u>Log σ(Ωcm)⁻¹</u>
0	-2.51
1.10	-2.75
2.55	-2.99
3.34	-3.05
4.02	-3.03
4.94	-2.93
6.01	-2.74
6.42	-2.65
7.40	-2.42
7.96	-2.29
8.78	-2.10
10.25	-1.74
11.20	-1.52
12.70	-1.18
13.91	-0.92
14.73	-0.76
15.98	-0.53
16.94	-0.37
17.96	-0.21

TABLE 11: The Conductivity Data for Undoped ST0.995.
 Quenched from a sintering temperature of
 1400°C

<u>-Log PO₂ (atm.)</u>	<u>Log σ(Ωcm)⁻¹</u>
0	-2.17
1.24	-2.45
2.07	-2.64
2.59	-2.74
3.50	-2.90
4.66	-3.01
6.00	-3.00
7.07	-2.90
8.35	-2.64
9.13	-2.45
10.20	-2.19
11.30	-1.90
12.69	-1.59
13.90	-1.28
14.74	-1.09
15.96	-0.80
17.00	-0.58
18.08	-0.42

TABLE 12: The Conductivity Data for Undoped ST0.995.

<u>-Log PO₂ (atm.)</u>	<u>Log σ(Ωcm)⁻¹</u>
0	-2.26
1.26	-2.54
2.06	-2.72
2.61	-2.82
3.37	-2.95
4.50	-3.04
5.76	-2.99
7.21	-2.80
8.49	-2.51
9.38	-2.29
10.58	-2.00
11.45	-1.79
12.61	-1.53
13.90	-1.24
14.74	-1.05
15.97	-0.77
16.98	-0.58
18.05	-0.41

TABLE 13: The Conductivity Data for Undoped ST0.995. Quenched from a sintering temperature of 1470°C.

<u>-Log PO₂ (atm.)</u>	<u>Log σ (Ωcm)⁻¹</u>
0	-2.00
1.08	-2.25
2.06	-2.48
2.75	-2.63
3.40	-2.75
4.50	-2.92
4.99	-2.97
5.39	-2.99
5.99	-2.99
6.79	-2.94
7.67	-2.83
8.26	-2.72
9.11	-2.55
10.45	-2.25
11.12	-2.09
12.46	-1.77
13.89	-1.43
14.72	-1.23
15.97	-0.94
16.97	-0.71
18.02	-0.47

TABLE 14: The Conductivity Data for Undoped ST0.990.

<u>-Log PO₂ (atm.)</u>	<u>Log σ(Ωcm)⁻¹</u>
0	-2.06
1.07	-2.31
2.05	-2.53
2.50	-2.62
3.27	-2.76
4.45	-2.91
5.39	-2.94
6.24	-2.89
7.51	-2.70
8.83	-2.42
10.11	-2.11
11.12	-1.87
12.38	-1.57
13.92	-1.21
14.74	-1.03
15.98	-0.76
16.96	-0.55
17.98	-0.34

TABLE 15: The Conductivity Data for Undoped ST0.900.

<u>-Log PO₂ (atm.)</u>	<u>Log σ(Ωcm)⁻¹</u>
0	-2.05
1.04	-2.30
2.07	-2.52
2.64	-2.63
4.55	-2.91
5.18	-2.94
6.12	-2.89
6.75	-2.82
7.76	-2.64
8.43	-2.50
9.16	-2.34
10.46	-2.02
11.17	-1.85
12.18	-1.62
12.69	-1.49
13.91	-1.21
14.71	-1.03
16.96	-0.55
18.02	-0.34

TABLE 16: The Conductivity Data for Undoped ST0.810.

<u>-Log PO₂ (atm)</u>	<u>Log σ(Ωcm)⁻¹</u>
0	-2.07
1.12	-2.32
2.05	-2.51
2.94	-2.66
4.51	-2.84
5.14	-2.84
6.46	-2.71
7.40	-2.57
8.52	-2.34
10.46	-1.90
11.15	-1.74
12.64	-1.38
13.88	-1.10
14.71	-0.91
16.02	-0.63
16.95	-0.44
18.01	-0.25

TABLE 17: The Conductivity Data for Undoped ST1.002.

<u>-Log PO₂ (atm.)</u>	<u>Log σ(Ωcm)⁻¹</u>
0	-2.41
1.09	-2.64
2.08	-2.84
2.75	-2.94
3.48	-3.01
3.97	-3.03
4.62	-3.01
5.53	-2.92
6.90	-2.71
8.17	-2.44
8.95	-2.26
10.26	-1.95
11.25	-1.71
12.70	-1.37
13.87	-1.13
14.70	-0.97
15.96	-0.73
16.94	-0.54
17.97	-0.31

TABLE 18: The Conductivity Data for Undoped ST1.005.

<u>-Log P_{O₂} (atm.)</u>	<u>Log σ(Ωcm)⁻¹</u>
0	-2.43
1.06	-2.66
2.03	-2.84
3.30	-3.02
5.58	-2.96
7.20	-2.65
7.88	-2.48
8.87	-2.21
17.02	-0.52
17.89	-0.35

TABLE 19: The Conductivity Data for ST1005-10000 Al.

<u>-Log PO₂ (atm.)</u>	<u>Log σ(Ωcm)⁻¹</u>
0	-1.51
1.34	-1.81
2.05	-1.96
2.18	-1.98
2.78	-2.10
3.55	-2.24
4.71	-2.42
5.46	-2.52
6.34	-2.58
7.53	-2.62
7.75	-2.62
8.24	-2.62
9.00	-2.59
9.41	-2.57
10.40	-2.49
11.17	-2.40
12.66	-2.16
13.89	-1.91
14.70	-1.74
15.98	-1.44
16.98	-1.21
17.97	-0.96

TABLE 20: The Conductivity Data for ST0.995-10000 Al.

<u>-Log PO₂ (atm.)</u>	<u>Log σ(Ωcm)⁻¹</u>
0	-1.60
1.04	-1.84
2.07	-2.06
2.70	-2.18
3.51	-2.32
4.59	-2.48
5.77	-2.59
7.24	-2.64
7.98	-2.64
9.10	-2.59
10.29	-2.46
11.01	-2.36
12.70	-2.06
13.91	-1.80
14.72	-1.61
16.01	-1.31
16.99	-1.06
18.00	-0.80

TABLE 21: The Conductivity Data for BT 0.995-10000 Al.

<u>-Log PO₂ (atm.)</u>	<u>Log σ(Ωcm)⁻¹</u>
0	-1.79
1.08	-2.04
2.07	-2.25
2.80	-2.40
3.33	-2.49
4.46	-2.68
5.45	-2.74
6.29	-2.70
6.74	-2.66
7.21	-2.60
7.79	-2.51
8.55	-2.36
9.69	-2.10
11.16	-1.77
12.69	-1.41
13.91	-1.13
14.73	-0.95
15.99	-0.67
16.92	-0.48
17.90	-0.28

TABLE 22: The Conductivity Data for ST0.995-10000 Nb.

<u>-Log PO₂ (atm.)</u>	<u>Log σ(Ωcm)⁻¹</u>
0	-0.53
1.11	-0.53
4.36	-0.53
8114	-0.53
10.33	-0.53
11.00	-0.53
12.62	-0.51
13.92	-0.47
14.76	-0.42
16.06	-0.30
17.03	-0.21
18.07	-0.09

TABLE 23: The Conductivity Data for ST0.995-5000 Nb.

<u>-Log PO₂ (atm.)</u>	<u>Log $\sigma(\Omega\text{cm})^{-1}$</u>
0	-1.71
2.08	-1.69
3.86	-1.66
4.91	-1.63
6.04	-1.55
7.92	-1.47
8.37	-1.43
11.17	-1.18
12.67	-0.98
13.88	-0.81
14.73	-0.69
15.99	-0.50
16.97	-0.35
17.97	-0.19

TABLE 24: The Conductivity Data for ST0.995-15000 Nb.

<u>-Log PO₂ (atm.)</u>	<u>Log σ(Ωcm)⁻¹</u>
0	-2.37
1.05	-2.11
4.23	-1.36
6.96	-0.79
8.88	-0.52
10.22	-0.33
10.91	-0.25
12.65	-0.08
14.69	+0.08
15.98	+0.18
16.94	+0.26
17.93	+0.36

TABLE 25: The Conductivity Data for ST0.995-20000 Nb.

<u>-Log P_{O₂} (atm.)</u>	<u>Log σ (Ωcm)⁻¹</u>
0	-2.63
1.18	-2.35
2.06	-2.14
2.95	-1.94
3.34	-1.85
4.54	-1.62
5.93	-1.26
7.57	-0.95
8.84	-0.71
8.90	-0.69
10.21	-0.45
10.31	-0.43
13.88	+0.17
17.96	+0.67

TABLE 26: The Conductivity Data for ST0.995-30000 Nb.

<u>-Log PO₂ (atm.)</u>	<u>Log σ(Ωcm)⁻¹</u>
0	-2.63
1.14	-2.36
2.93	-1.94
4.39	-1.65
8.99	-0.69
11.47	-0.23
12.64	-0.03
13.90	+0.16
14.73	+0.30
15.98	+0.46
18.01	+0.67

TABLE 27: The Conductivity Data for ST0.995-2000 Nb.

<u>-Log PO₂ (atm.)</u>	<u>Log σ(Ωcm)⁻¹</u>
0	-2.62
1.18	-2.83
2.05	-2.96
2.99	-2.99
3.59	-2.97
4.70	-2.82
5.75	-2.59
6.87	-2.36
8.13	-2.10
8.87	-1.96
10.31	-1.64
11.20	-1.44
12.63	-1.17
13.90	-0.93
14.72	-0.78
15.95	-0.57
16.96	-0.40
17.97	-0.23

VITA

Stefan Witek was born on August 29, 1957, in Mansfield, England. He attended Queen Elizabeth's Grammar School where he passed 'O'-level examinations in Maths, Physics, Chemistry, Biology, Classical Studies, English Language, History, French, in June 1973, and 'A'-level examinations in Maths, Physics, Chemistry, General Studies, in June 1975. At Leeds University he obtained a BSc. Hons. Degree (Class I) in Ceramics in June 1978. After leaving Leeds he worked at the Standard Telecommunication Laboratories in Harlow, Essex, as a research engineer, where he was involved in the development of ceramic dielectrics for use in capacitors. In January 1981, he became a graduate student at Lehigh University, in the Department of Metallurgy and Materials Engineering, where he has studied until present for the degree of Master of Science.